Soils and Rocks
www.soilsandrocks.com
An International Journal of Geotechnical and Geoenvironmental Engineering
ISSN 1980-9743
ISSN-e 2675-5475

In-situ and laboratory characterisation of stiff and dense geomaterials for driven pile analysis and design

Tingfa Liu[1#], Ken Vinck[2], Emil R. Ushev[3], Richard J. Jardine[2]

Article

Keywords
Laboratory testing
Glacial till
Dense sand
Chalk
Driven piles
Offshore Engineering

Abstract

Integrated field and laboratory characterisation of geomaterial behaviour is critical to foundation analysis and design for a wide range of offshore and onshore infrastructure. Challenges include the need for high-quality sampling, addressing natural and induced micro-to-macro structures, and applying soil and stress states that represent both *in-situ* and *in-service* conditions. This paper draws on the Authors' recent research with stiff glacial till, dense marine sand and low-to-medium density chalk, and focuses particularly on these geomaterials' mechanical behaviour, from small strains to failure, their anisotropy and response to cyclic loading. It considers a range of *in-situ* techniques as well as highly instrumented monotonic and cyclic stress-path triaxial experiments and hollow cylinder apparatus tests. The outcomes are shown to have important implications for the analysis of large driven piles under monotonic-and-cyclic, axial-and-lateral loading, and the development of practical design methods. Also highlighted are the needs for approaches that integrate field observations, advanced sampling and laboratory testing, numerical and theoretical modelling.

1. Introduction

The potential capabilities and practical values of advanced laboratory testing have been demonstrated through ISSMGE TC101's International Symposia (IS) from Hokkaido 1994 to Glasgow 2019. Jardine (2014, 2020, 2023a) highlighted their application with large piles driven to support key offshore and onshore infrastructure, noting that geomaterial behaviour under *in-situ* and *in-service* conditions can be affected markedly by pile installation effects as well as operational and extreme loading. Representative numerical analyses rely critically on experiments that match these conditions faithfully to provide the fundamental physical basis for constitutive model development and calibration (Zdravković et al., 2021).

The worldwide drive for renewable offshore wind energy has prompted large-scale research projects to tackle offshore wind foundation design challenges; those involving advanced soil characterisation include the PISA (Byrne et al., 2017), PICASO (Byrne et al., 2020a), WAS-XL (Page et al., 2021) ALPACA and ALPACA Plus (Jardine et al., 2023b) projects. High-quality pile test databases have also been collated by Yang et al. (2017) and Lehane et al. (2020, 2022).

Establishing the behaviour of dense marine sands, stiff glacial tills, Eocene to Jurassic stiff clays and chalks has been particularly significant in developing large concentrations of offshore windfarms around the UK and northern European coastlines where such strata are often encountered. This requires: (i) high quality sampling (Hight & Jardine 1993); (ii) addressing both natural geomaterials' properties and potential alterations induced by pile driving and soil-pile interaction; and (iii) applying appropriate effective stress states and perturbing stress paths (Jardine, 2014). This paper draws on contributions made to the PISA, ALPACA and ALPACA Plus Joint Industry Projects (JIPs) by Liu (2018), Ushev (2018) and Vinck (2021). The experiments conducted on the three formations considered below have contributed to making significant improvements in offshore wind turbine foundation design.

- **Cowden clay**, stiff, high Yield Stress Ratio (*YSR*, or apparent *OCR*) sandy glacial till sampled at the PISA test site, NE England;
- **Dunkirk sand**, fine marine predominately silica sand from the PISA site in Northern France, consisting of dense to very dense normally consolidated hydraulic fill (average relative density $D_R \approx 100\%$) and Flandrian sand (average $D_R \approx 75\%$);
- **St Nicholas at Wade (SNW) chalk**, low-to-medium density B2/B3 grade Margate and Seaford chalk from the Upper Cretaceous sampled at the ALPACA site in Kent, SE England.

[#]Corresponding author. E-mail address: tingfa.liu@bristol.ac.uk
[1]University of Bristol, School of Civil, Aerospace and Design Engineering, Bristol, United Kingdom.
[2]Imperial College London, Department of Civil and Environmental Engineering, London, United Kingdom.
[3]Wood Thilsted, London, United Kingdom.

Submitted on August 23, 2023; Final Acceptance on February 19, 2024; Discussion open until November 30, 2024.
https://doi.org/10.28927/SR.2024.009323

An overview of the ground conditions at these sites is presented, before considering three topics for each geomaterial:

- Mechanical behaviour from very small to large strains, emphasising non-linearity, anisotropy as well as rate-and-time dependency, interpreted within suitable frameworks;
- Synthesis of *in-situ* and laboratory measurements;
- The geomaterials' response to drained or undrained cyclic loading.

Mention is made briefly of how soil-steel interface behaviour is affected by stress level, time (ageing), displacement, surface roughness, pore water chemistry and other conditions. Attention is also drawn to how field and laboratory testing can be applied in analyses of impact driven piles subjected to general loading.

2. Geotechnical overview

2.1 Site profiles

Cowden site encounters Bolders Bank formation glacial tills, whose deposition involved cycles of ice loading and horizontal shearing and/or glaciotectonic passive pressures (Davies et al., 2011). The till comprises principally stony, sandy and silty clay units that under-drain into two sand layers (Powell & Butcher, 2003; Ushev, 2018; Zdravković et al., 2020a; Ushev & Jardine, 2022a). While a water table is encountered at 1.0 m depth, pore-pressures become under-drained at depth. The till's index properties are summarised in Table 1 and Figure 1. Figure 2a presents typical profiles of corrected Cone Penetration Test (CPTu) resistances (q_t); the occasional spikes indicate hard stone inclusions. Triple-barrel, wireline, Geobore-S rotary coring and block sampling campaigns retrieved a sufficient stock of high-quality intact specimens, although the till's stony nature and 8% gravel content limited the core recovery rate to ≈ 42%.

Dunkirk conditions consist of mainly normally consolidated marine Flandrian sands down to the Ypresian Eocene marine clay found at 30 m (Brucy et al., 1991; Chow, 1997; Jardine et al., 2006; Zdravković et al., 2020a). Three metres of hydraulic sand fill of the same origin were placed over the Flandrian sands in the 1970s without compaction or surcharging. Particle size analyses indicate uniform fine-to-medium sand; see Figure 1. The sub-angular particles comprise ≈ 85% silica, plus calcium carbonate ($CaCO_3$) shell fragments and other minerals that leave the soil slightly alkaline (Chow, 1997). Table 1 summarises index properties, after Kuwano (1999) and Aghakouchak (2015). The site's q_t profiles are illustrated in Figure 2b. Groundwater was encountered at 5.4 m in 2014, 1.4 m deeper than that found by Chow (1997) with hydrostatic conditions below. While rotary coring was conducted for Brucy et al.'s (1991) investigation, coring for PISA was unsuccessful due to disturbance and drilling fluid contamination. The laboratory testing therefore had to rely on reconstituted bulk samples.

St Nicholas at Wade (SNW) The chalk site was characterised by Diambra et al. (2014) and Ciavaglia et al. (2017) prior to Buckley's (2018) and Buckley et al. (2018) investigations for the Innovate UK project and the exhaustive ALPACA and ALPACA Plus studies (Vinck, 2021; Vinck et al., 2022; Jardine et al., 2023c). Pure (98.6% $CaCO_3$) white Margate Chalk was found down to the Barrois' Sponge Bed at 5.2 m Above Ordnance Datum (AOD) above the Seaford white Chalk. The chalk classifies as CIRIA Grade B3/B2 (structured, very weak to weak, low-to-medium density) over the depths of interest, with discontinuity apertures < 3 mm and fractures spaced at 60 to 600 mm. Predominantly vertical linear micro-fissures were identified at all depths with ≈ 10 to 25 mm spacings. The ALPACA team located the (fresh) water table ≈ 0.9 m AOD, with ±

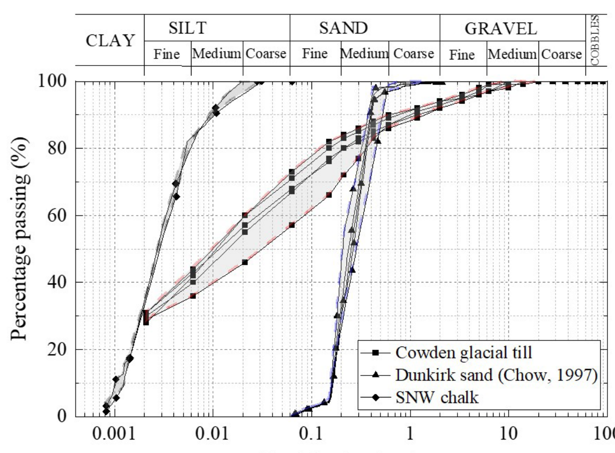

Figure 1. Particle size distributions of Cowden till, Dunkirk sand and SNW chalk over the depths of interest.

Table 1. Typical index properties of the three geomaterials.

Material	D_{50} (mm)	G_s	wc (%)	w_P (%)	w_L (%)	ρ_{bulk} (g/cm³)
Cowden glacial till	0.01-0.03	2.707-2.723	16.1-20.2	14.0-23.0	32.0-45.0	1.95-2.25
Dunkirk sand	0.21-0.28	2.65-2.66	5-7 (above WT) 22.7 (Below WT)	NA	NA	1.74 (above WT) 2.03 (below WT)
SNW chalk	0.003	2.71	27.9-33.0	22.3-23.9	30.2-32.0	1.85-1.98

Note: 'NA': Not Applicable.

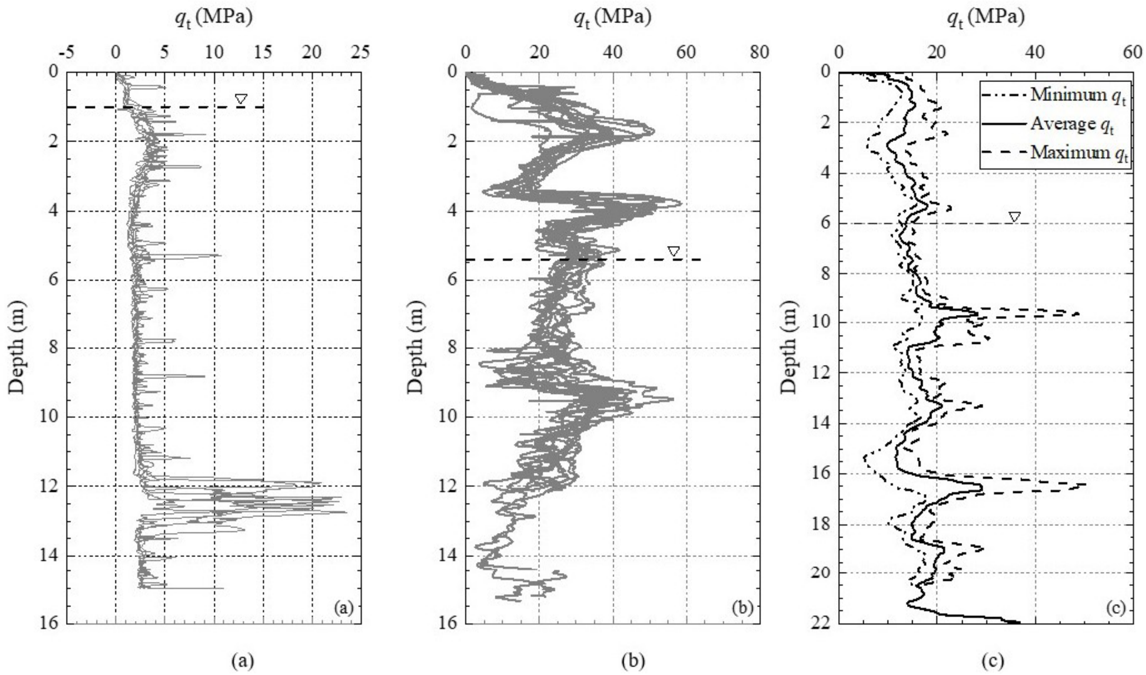

Figure 2. Corrected cone resistances (q_t) profiles for (a) Cowden, (b) Dunkirk and (c) St Nicholas at Wade (SNW) sites.

0.25 m variations. The chalk grains classify as fine silts (D_{50} 3-4 µm) with 1.43 Mg/m^3 to 1.53 Mg/m^3 Intact Dry Densities (IDD) and a 0.91 average liquidity index; see Table 1.

Typical CPTu profiles are presented in Figure 2c, showing 'spikes' in thin flint bands. Significant chalk de-structuration beneath and around CPT tips leads to excess pore pressures up to 10 MPa at u_1 (face) piezocone positions (Buckley, 2018) and ≈ 4 MPa at u_2 (shoulder) locations. Friction sleeve resistances indicate the chalk's partial de-structuration towards the soft 'putty' found around driven pile shafts. CPTu dissipation tests generally showed t_{50} times < 10 s from which Vinck et al. (2022) interpreted *in-situ* consolidation coefficients. Geobore-S rotary coring retrieved samples to ≈ 16 m depth, although the chalk's fractured and brittle nature limited the solid core recovery rate to 51% and a rock quality designation of 32%. Large block samples were taken from a 4 m deep excavated pit.

2.2 Test equipment

The Imperial College London laboratory testing employed fully instrumented automated Bishop-Wesley type triaxial cells for 38 mm and 100 mm diameter specimens. Liu et al. (2022a) detail the equipment and their stress and strain sensors' resolutions and precisions. The LVDTs employed to measure local strains offered resolutions ≈ 0.1 µm. Mid-height sensors tracked local pore water pressures in the Cowden tests and lubricated top and base platens were deployed in most tests (Vinck et al., 2019). Liu (2018) and Liu et al. (2020) provide full details of the Hollow Cylinder Apparatus (HCA) and Bishop ring shear apparatuses employed in parallel testing campaigns; supplementary experiments were undertaken at other research and commercial laboratories.

3. Cowden till

The PISA Cowden campaign first established profiles of index properties and oedometer test outcomes. Comparisons between the 1-D compression behaviours of natural and reconstituted specimens indicated a dense and insensitive natural fabric. Initial triaxial tests also provided information on the till's initial linear elastic response through to large-strain critical states that fed into finite element modelling. Liu (2018) and Ushev (2018) extended the scope to investigate the till's anisotropy, strain rate and pressure dependent monotonic shearing behaviour, as well its undrained cyclic loading response, while Ushev & Jardine (2022a) explored the till's large-displacement soil-soil and soil-steel interface shearing characteristics.

3.1 Index and mechanical property profiles

The Cowden till comprises predominantly low plasticity (plastic limit ≈ 14-23%) clay over the depth of interest; the 1.95 Mg/m^3 – 2.25 Mg/m^3 bulk densities reflect its gravel content. Figure 3a plots the 1-D compression yield stresses, σ_{vy}', and Yield Stress Ratio (YSR, or apparent $OCR = \sigma_{vy}'/\sigma_{v0}'$) profiles from stage-loaded and constant rate of compression

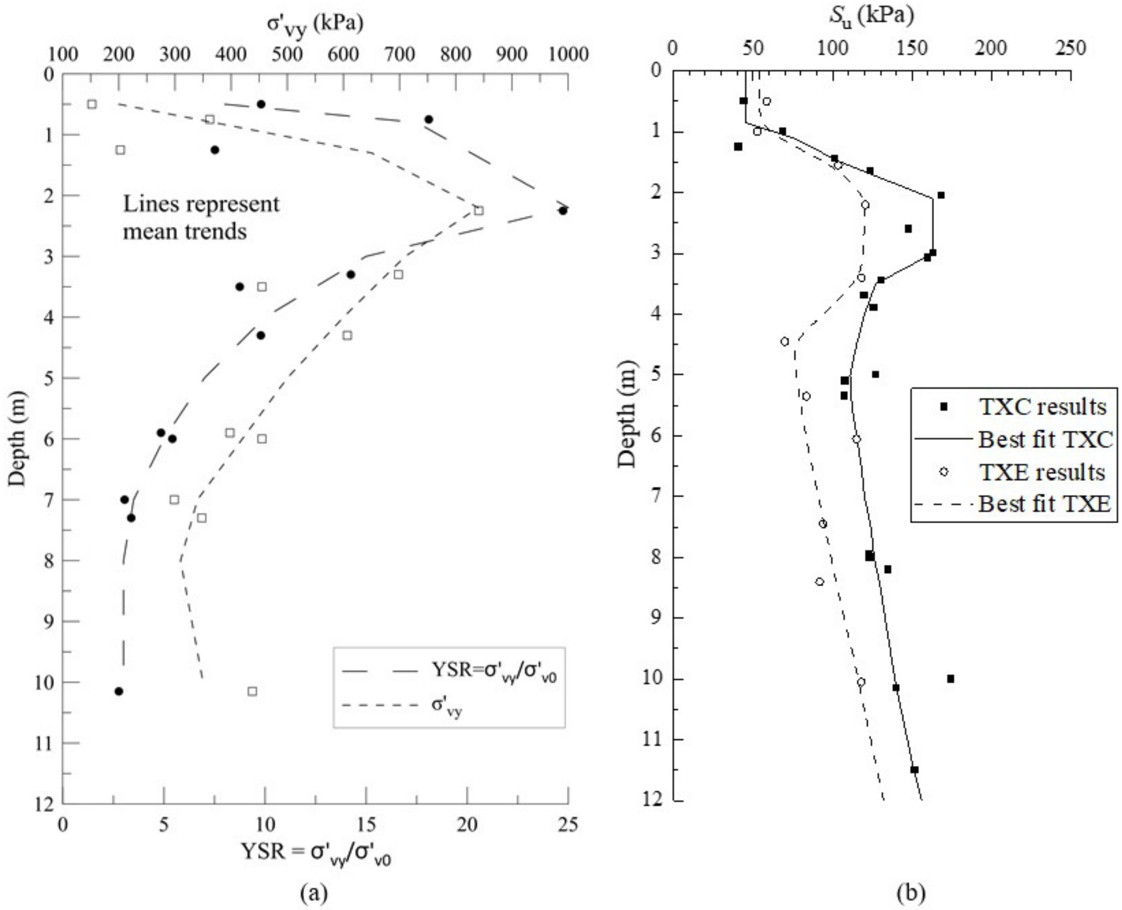

Figure 3. Cowden site profiles of (a) 1-D yield stress σ_{vy}' and *YSR* and (b) S_u from triaxial compression (TXC) and extension (TXE) tests; all tests performed on high-quality intact specimens (modified from Liu et al., 2020; and Ushev & Jardine, 2022a, b).

oedometer tests. The high YSRs noted over the upper 4 m reflect complex glacial and post-glacial processes. Although Powell & Butcher (2003) interpreted K_0 values exceeding 2.5 from various empirical procedures, Jardine (1985) argued that glacial lodgement till deposition leads to lower K_0 values that are more compatible with the networks of open vertical fissures observed especially within the desiccated and more stony upper sections. Therefore, the laboratory triaxial tests and analyses limited K_0 to 1.5 within the upper 7 m and unity below this depth.

The peak undrained triaxial compression and extension strengths (S_u) of natural specimens re-consolidated to *in-situ* stresses are reported in Figure 3b. The profiles exhibit similar shapes that, like the oedometer σ_{vy}' profile in Figure 3a, differ markedly from the patterns expected in gravitationally consolidated waterborne sediments after monotonic geostatic loading and unloading. The compression profile indicates an average CPT $N_{kt} \approx 18$, while the average S_u^{TXC}/S_u^{TXE} ratio is 1.25. Liu et al. (2020) argue that the latter ratio does not reflect the till's anisotropy because the extension strengths are affected by necking and different Lode angles (or *b* values) applied in compression and extension. Liu et al. (2020, 2023a) report HCA experiments that investigated the till's anisotropy more rigorously.

3.2 Triaxial monotonic shearing

3.2.1 Stiffness

The triaxial tests addressed behaviour from strains of 10^{-6} up to ultimate failure with deviatoric strains ε_s >25%. The natural Cowden till only exhibited elastic behaviour under small stress and strain increments, no greater than a few kPa and 0.002% respectively, that remained within the till's Y_1 kinematic yield surface (Jardine, 1992). Undrained vertical Young's moduli established by regression analyses of these initial portions led to the E^u_{sec} profile in Figure 4a along with secant stiffness profiles for axial (or ε_s) levels of 0.001%, 0.01%, 0.1% and 1%, which indicate nearly parabolic trends with depth. Analysis confirmed that E^u scales with p' raised to a partial power, as expressed in Equation 1, where p_{ref} is atmospheric pressure. The exponent β can be taken as 0.5 and the α values are largely constant with depth for each strain level;

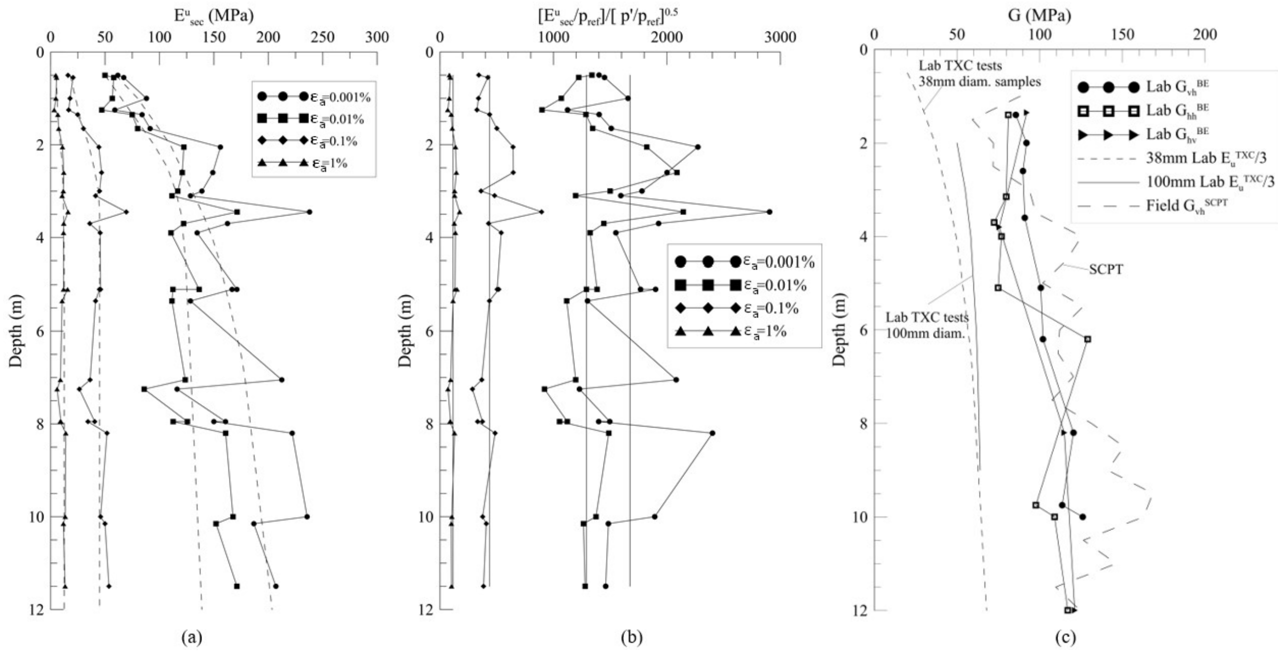

Figure 4. Cowden stiffness profiles of: (a) triaxial compression secant stiffness E^u_{sec} at axial strains of 0.001%, 0.01%, 0.1%, and 1%; (b) normalised triaxial secant stiffness $[E^u_{sec}/p_{ref}]/[p'/p_{ref}]^{0.5}$ at four axial strain levels, applying Equation 1 with $\beta = 0.5$; and (c) elastic shear stiffnesses from laboratory and field geophysical measurements, with $E_u^{TXC}/3$ profile from triaxial compression tests (modified from Ushev & Jardine, 2022a).

see Figure 4b. Similar traces were observed for the interpreted triaxial tangent Young's moduli (E^u_{tan}) (Ushev, 2018).

$$E^u = \alpha\, p_{ref} \left(\frac{p'}{p_{ref}} \right)^{\beta} \tag{1}$$

Figure 5 shows the degradation of normalised secant stiffness $[E^u_{sec}/p_{ref}]/[p'/p_{ref}]^{0.5}$ with strain, with degradation being steeper in extension than in compression.

As discussed in greater detail later, Cowden till shows cross-anisotropic stiffnesses. Figure 4c plots laboratory bender element G_{vh}, G_{hv} and G_{hh} profiles for intact specimens along with in-situ seismic CPT (SCPT) G_{vh} data from Zdravković et al. (2020a). The laboratory and SCPT G_{vh} traces plot relatively close together, although the field values are (on average) slightly higher. Also shown in Figure 4c is the equivalent isotropic octahedral shear moduli G_{oct} taken as $E_u^{TXC}/3$ which falls far below the bender element G_{vh} *and* G_{hh} trends because of the till's anisotropy.

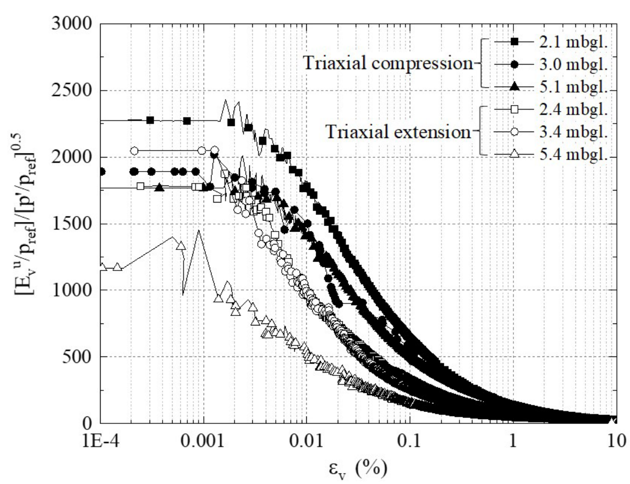

Figure 5. Typical degradation trends for normalised vertical secant undrained Young's moduli from anisotropically consolidated triaxial compression and extension tests on intact Cowden till from upper layers (modified from Liu et al., 2020).

3.2.2 Large-strain yielding and rate-dependent behaviour

Cowden till exhibits ductile, strain hardening, triaxial compression behaviour. Stable failure states were reached after imposing large strains, with the specimens' barrelling without any evident shear banding. These points were interpreted as critical states with $M^{TXC} = q/p'$ around 1.0, equivalent to $\phi_{cs}' = 25.4°$, $c' = 0$ and applied in constitutive modelling of the till. Figure 6 shows typical undrained effective stress paths from compression (TXC) and extension (TXE) tests in q-p' ($q = (\sigma_v' - \sigma_h')$, $p' = (\sigma_v' + 2\sigma_h')/3$) coordinates. Also indicated are large-scale 'Y_3 yield points' interpreted as the points (at $q \approx 100$ kPa) where the effective stress paths rotated from their initial negative $dp'/$

dq ratios (that reflect the till's elastic stiffness anisotropy) to follow paths with positive, dilative, dp'/dq directions. While the TXC tests progressed to stable critical states, all TXE specimens developed necking failures which lead to apparently low peak shear strengths and post-peak softening. A notional Hvorslev surface is shown that runs from the final TXC critical state point back to the no-tension cut-off and encompasses the large strain undrained effective stress paths. Similar critical states and Hvorslev surfaces were assumed to apply in extension.

Noting that rapid lateral pile loading tests at Cowden delivered markedly higher peak loads and stiffness than slower stage-loaded experiments (Byrne et al., 2020b), Ushev (2018) investigated the till's rate-dependency. Triaxial tests run at axial strain rates of 5%/day, 50%/day and 500%/day showed S_u and secant stiffness increasing by ≈ 6% and 10% respectively per tenfold rate change. Compatible rate trends and reversible isotach behaviour were observed in other tests that alternated between 5% and 500%/day shearing rates.

3.3 Anisotropic stiffness and shear strength characteristics

Differences observed in the till's triaxial compression and extension shear strengths and the triaxial and field stiffness profiles in Figures 3 and 4 prompted Liu et al. (2020) to investigate the till's stiffness anisotropy. Suites of triaxial probing tests on samples from 4 depths applied drained vertical ($d\sigma_v'$), horizontal ($d\sigma_h'$) and undrained vertical (dq) stress increments (of typically 2 kPa) at rates of 0.1-0.2 kPa/hour established the till's stiffness anisotropy. A suite of undrained HCA '$\alpha_{d\sigma}$-controlled' experiments that achieved five final σ_1 axis orientations with respect to the vertical (α_f values) spaced equally between 0 and 90˚. HCA simple shear (HCASS) and HCA triaxial compression tests (HCA TXC) performed on block sample specimens from 2.9 m established in this way the till's anisotropy up to shear failure. The $\alpha_{d\sigma}$-controlled and HCASS tests were controlled to keep the intermediate principal stress parameter (b) close to 0.5.

3.3.1 Cross-anisotropic elastic stiffnesses

Treating the till's linear elastic behaviour as cross-anisotropic and strain-rate independent allows dynamic and static measurements to be considered as compatible and inter-comparable. The cross-anisotropic stiffness matrix has five independent parameters, E_v', E_h', ν_{hv}' (or ν_{vh}'), G_{vh}, G_{hh} (or ν_{hh}') that can be determined experimentally (see for example Kuwano & Jardine, 2002). Three independent parameters, E_v^u, E_h^u and G_{vh} apply under undrained conditions that can be established from the drained set (see Brosse et al., 2017) or the combined drained and undrained probing approach proposed by Nishimura (2014) that places emphasis on the higher quality axial strain measurements.

The profiles with depth of G_{hh}/G_{vh}, E_h'/E_v' and E_h^u/E_v^u derived from Liu et al.'s (2020) triaxial and HCA tests plotted in Figure 7 show a generally consistent trend for a stiffer response under horizontal than vertical loading, which is

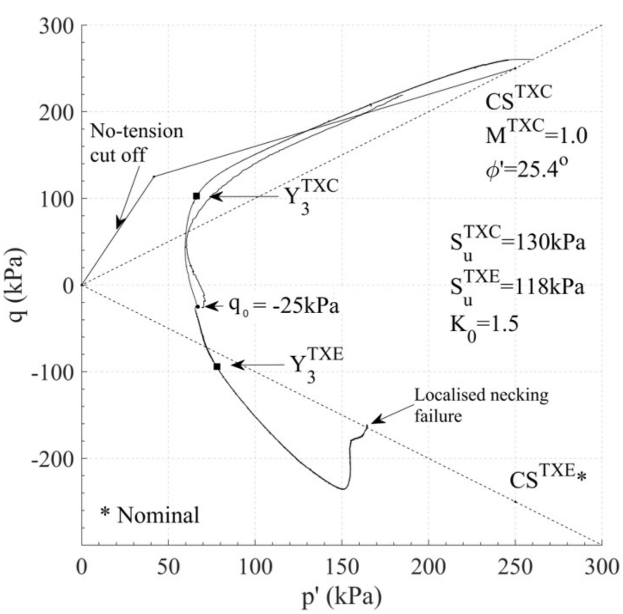

Figure 6. Typical undrained triaxial compression and extension effective stress paths for Cowden till samples from 3.0 to 3.5 m depth (Axial shear strain rate: 5%/day) (modified from Ushev & Jardine, 2022b).

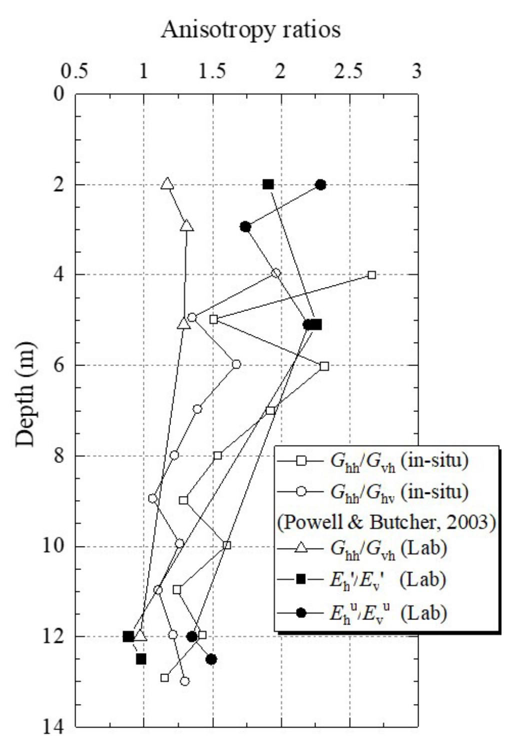

Figure 7. Anisotropic stiffness ratio profiles for Cowden site (modified from Liu et al., 2020).

important to recognise when analysing lateral pile loading. Also shown are G_{hh}/G_{vh} and G_{hh}/G_{hv} ratios from in-situ down-hole and cross-hole shear velocity tests by Powell & Butcher (2003); stiffness anisotropy clearly diminishes with depth.

3.3.2 Non-linear stiffness characteristics over full strain range

Following Brosse et al. (2017), the $\alpha_{d\sigma}$-controlled Cowden HCA tests allowed undrained vertical and horizontal Young's moduli and torsional shear stiffness to be tracked over a wide strain range. The till's marked elastic-plastic stiffness degradation under HCA conditions is demonstrated in Figure 8 by plotting E_v^u and E_h^u against vertical strain ε_z and average horizontal strain $(\varepsilon_r + \varepsilon_\theta)/2$, respectively. Despite showing initial scatter, the moduli exhibit consistent degradation trends. Narrow spreads apply to each component, suggesting that the cross-anisotropic stiffness components are relatively insensitive to the shearing path followed. The two HCA triaxial tests, which employed pre-shearing $b = 1.0$ and ultimate $b_u = 0$, showed overlapping E_v^u trends that fall slightly below those of most $b = 0.5$ tests. Overall, the E_h^u curves plot above the E_v^u data trends, confirming that stiffness anisotropy persists as strains grow.

When taken to failure, under nominally plane strain conditions, in HCA tests, the highest shear strengths developed when σ_1 acted horizontally ($b = 0.5$, $\alpha_f = 90°$) and the lowest when σ_1 acted vertically; the shear strengths specimens applying at intermediate α_f values spanned these limits, confirming that any S_u anisotropy inferred from comparing triaxial compression and extension strengths (see Figure 3b) would be misleading.

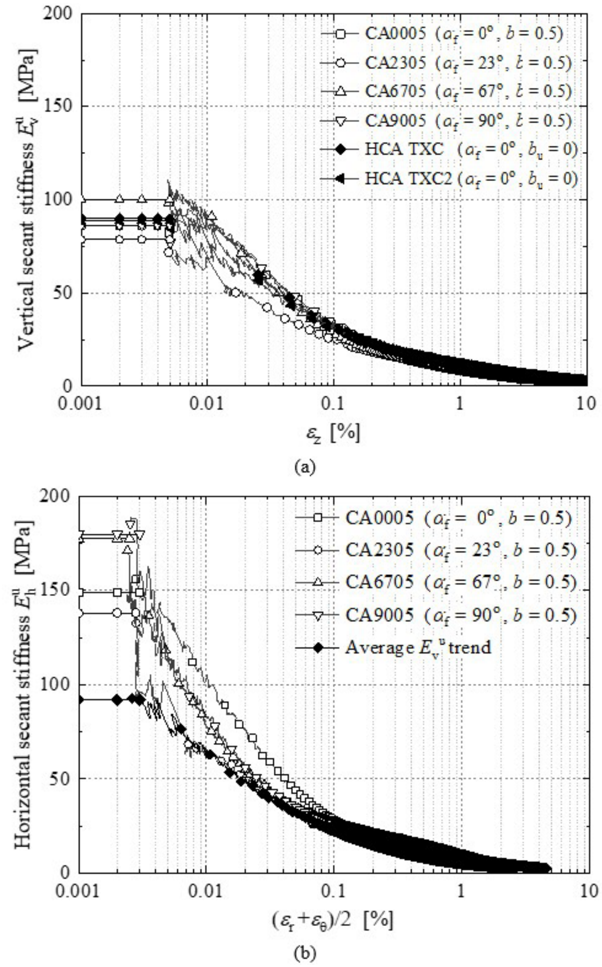

Figure 8. Cowden stiffness degradation from HCA tests: (a) undrained vertical secant Young's moduli E_v^u against vertical (axial) strain; (b) undrained horizontal secant Young's moduli E_h^u against mean horizontal strain (modified from Liu et al., 2020).

3.4 Response to undrained cyclic loading

Cyclic loading, which can be critical for offshore structures, was addressed in the PISA field pile testing. Ushev (2018) and Ushev & Jardine (2022b) supported this work by investigating Cowden till's response to undrained triaxial cyclic loading, considering multiple nominally identical samples from 3.4 mbgl re-consolidated to in-situ stresses q_0 = -25 kPa, p_0' = 67 kPa. Mean (q_{mean}) and cyclic (q_{cyc}) deviatoric stresses, in the -25 to 200 kPa and 10 to 150 kPa respective ranges, were applied to populate the q_{mean}-q_{cyc} interactive loading plane and investigate how the combinations affected the evolving trends for effective stress, cyclic strain and stiffness, damping ratios and any cyclic failures.

3.4.1 Number of cycles to failure and cyclic interaction diagram

The influences of the mean q_{mean} and cyclic q_{cyc} deviatoric stresses were considered in both (i) the conventional total stress $q_{cyc}/(2S_u)$ and $q_{mean}/(2S_u)$ interactive loading space and (ii) alternative 'effective-stress' normalised $q_{cyc}/p'_{in\text{-}situ}$ and $q_{mean}/p'_{in\text{-}situ}$ space, as shown in Figure 9. Five of the higher amplitude cyclic tests failed after the indicated number of cycles (N_f). All other specimens remained un-failed when loading halted after 1500 to 3500 cycles. Interpreted contours are shown of the conditions under which failure can be expected at N_f = 10, 100 or 1000. A stable zone is indicated where cyclic failure is not expected within 1000 cycles, and regions where failures occurred by either (i) large cyclic and average strains that led to "abrupt failure" or (ii) mean strains accumulating and samples "creeping towards failure".

3.4.2 Evolution of effective stress, cyclic strain and stiffness

Cowden till's cyclic effective stress path and overall cyclic loading behaviour varied systematically with the normalised loading parameters. Typical 'stable' and 'unstable' responses are illustrated in Figure 10 for specimens cycled under q_{cyc} = 25 kPa and a single test involving q_{cyc} = 150 kPa from '*in-situ*' q_{mean} = -25 kPa. Also shown are the no-tension lines, the Hvorslev surfaces and *M* lines identified from the static tests. Figure 10a illustrates the stable outcomes of experiments involving q_{cyc} = 25 kPa ($q_{cyc}/(2S_u)$ = 0.1). Shifts can be seen from an initially "dilative" drift trend to one indicating slightly "contractive" behaviour. In contrast, the higher amplitude q_{cyc} = 100 and 150 kPa ($q_{cyc}/(2S_u)$ = 0.4 and 0.6) experiments conducted from q_{mean} = -25, 50 and 125 kPa all initially violated the 'slow shearing' Hvorslev surface and subsequently progressed to fail within 1000 cycles. One example is given in Figure 10b. The final stages of 'unstable' experiments could involve axial strain rates up to 200 times higher than the reference monotonic experiments, explaining why they were able to sustain transient conditions that could not be sustained under slow monotonic loading. The specimens' p' values fell more significantly on unloading than they rose during loading, leading to an overall contractive trend with the paths heading leftward towards the origin, developing irregular loops and broad "butterfly-wing" shapes.

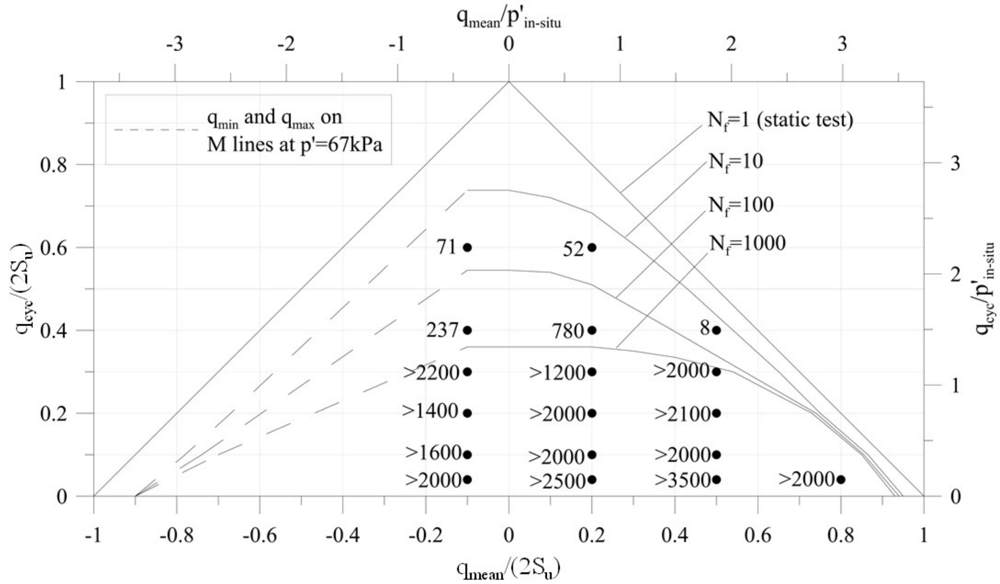

Figure 9. Contours of number of cycles to failure for intact Cowden till in normalised stress space (modified from Ushev & Jardine, 2022b).

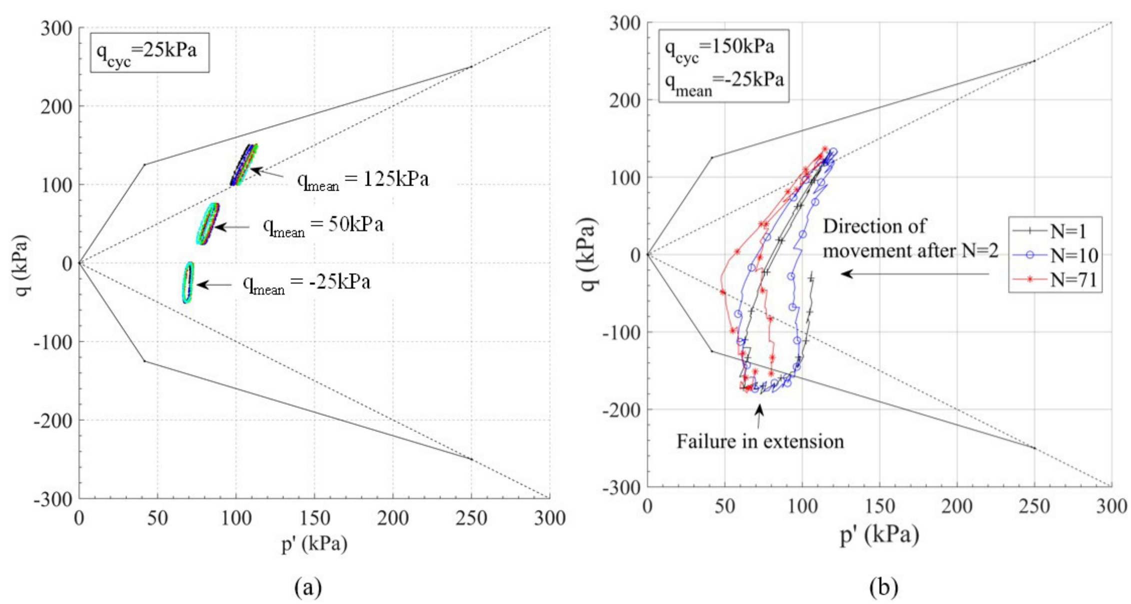

Figure 10. Effective stress paths of Cowden till under undrained cyclic triaxial shearing: (a) typical stable response under low amplitude cycling; (b) unstable cycling response under high q_{cyc} level of 150 kPa (Ushev & Jardine, 2022b; Liu et al., 2023a).

Typical patterns of permanent axial strain (ε_{mean}) accumulation with N are plotted in Figure 11a on logarithmic scales. The strains developed under the lowest (10 kPa) cyclic amplitudes tended to stabilise after 100 to 1000 cycles to rates comparable to the slow residual creep rates (< 0.005%/day) applying before cycling started. Empirical power law relationships were found that relate the strain development of stable and metastable tests to their normalised cyclic loading parameters. Figure 11b presents the cyclic peak-to-trough secant stiffnesses trends for tests performed at in-situ q_{mean}. The tests that manifested stable effective stress loops showed stiffness either growing slightly with N or falling modestly before stabilising; unstable cycling response led to cyclic stiffness falling sharply with N.

3.4.3 Cyclic kinematic yield surfaces

The cyclic responses observed in the stable and metastable tests can be related to two kinematic yield surfaces that, once engaged, move with the current effective stress point; Jardine (1992). The first elastic, Y_1, region is approximately elliptical in shape and has a maximum height of only about ± 2.5 kPa in-situ for the cyclic series' specimens. The second Y_2 kinematic yield surface (KYS), defined here as the threshold limit to: (i) stable effective stress conditions that involve less than 5% variation in p' over 2000 ± 500 cycles and (ii) practically constant cyclic stiffness. Figure 12 marks the approximate boundaries of the Y_1 (red circles) and Y_2 (black ellipses) surfaces that surround each q_{mean} point. The Y_2 surfaces' vertical dimensions diminished as the pre-loading effective conditions approached the Hvorslev surface, even though p' increased as the samples moved along this undrained loading path. While cyclic loading within the initial Y_2 kinematic yield surface does not appear deleterious, paths that engage Y_2 on each loading and unloading stages dissipate far more energy and provoke marked stiffness degradation and strain accumulation.

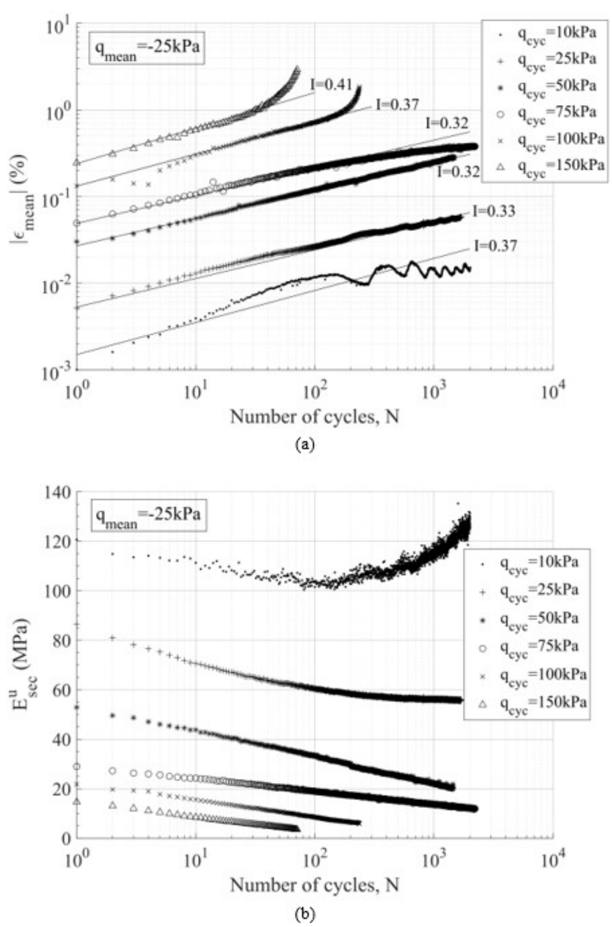

Figure 11. Evolution trends for (a) mean (permanent) axial strain and (b) cyclic secant stiffness against number of cycles for intact Cowden till specimen cycled from in-situ mean q_{mean} = -25 kPa (Ushev & Jardine, 2022b, Liu et al., 2023a).

4. Dunkirk sand

The Dunkirk PISA triaxial testing focused initially on calibrating the Taborda et al. (2014) state parameter-based bounding surface plasticity model employed to design and model lateral pile tests. The research scope extended later to consider stiffness anisotropy and long-term drained cyclic loading behaviour, again aiming to support cyclic pile tests. Liu (2018) and Liu et al. (2019a, b) report on the sand's interface shearing behaviour.

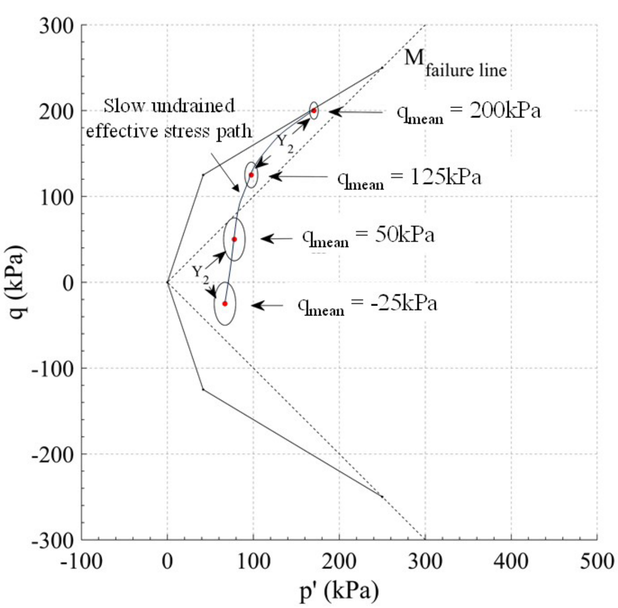

Figure 12. Y_2 kinematic yield surfaces for Cowden till interpreted from cyclic undrained triaxial tests at four mean deviatoric stress (q_{mean}) points along a slow compression test path to failure (modified from Ushev & Jardine, 2022a, b).

4.1 Site stiffness profiles

Extensive field SCPT and laboratory bender element and small-stress probing tests led to the stiffness profiles plotted in Figure 13. The 2016 PISA SCPT tests indicated higher G_{vh} profiles than those reported by Chow (1997) at a location 100 m distant, potentially reflecting local ground variability and/or the effects of ageing over ≈ 20 years under the hydraulic fill (Zdravković et al., 2020a). Drained triaxial tests indicated consistently higher vertical (E_v') than horizontal (E_h') moduli, reflecting the applied K_0 = 0.4, although the G_{vh} and G_{hh} components showed less difference. The *in-situ* SCPT G_{vh} profiles plotted distinctly above laboratory bender element (BE) values, especially above the water table, which was ascribed to long-term ageing, partial saturation *in-situ* and seasonal water table fluctuations. Checking for, and addressing, such discrepancies is crucial to successful practical modelling of laterally loaded monopiles.

4.2 Full strain mechanical behaviour under monotonic loading

4.2.1 Linear elastic stiffness anisotropy

Liu (2018) undertook stress-path probing tests on fully instrumented 100 mm diameter specimens that were consolidated and swelled along five constant K (= σ_h'/σ_v') stress ratio paths.

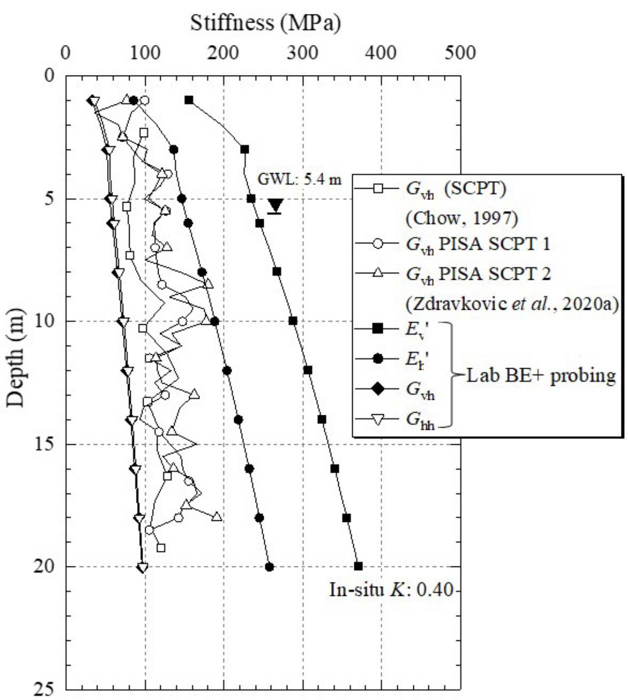

Figure 13. Dunkirk stiffness profiles from *in-situ* SCPT, laboratory bender element (BE) and triaxial small-stress probing tests (Liu, 2018).

The following functions were fitted to correlate the cross-anisotropic stiffnesses with the principal stresses σ_v' and σ_h'.

$$E_v' = f(e)C_v\left(\frac{\sigma_v'}{p_{ref}}\right)^{a_v} \tag{2}$$

$$E_h' = f(e)C_h\left(\frac{\sigma'}{p_{ref}}\right)^{b} \tag{3}$$

$$G_{vh} = f(e)C_{vh}\left(\frac{\sigma_v'}{p_{ref}}\right)^{a_{vh}}\left(\frac{\sigma_h'}{p_{ref}}\right)^{b_{vh}} \tag{4}$$

$$G_{hh} = f(e)C_{hh}\left(\frac{\sigma_v'}{p_{ref}}\right)^{a_{hh}}\left(\frac{\sigma_h'}{p_{ref}}\right)^{b_{hh}} \tag{5}$$

where C_v, C_h, C_{vh}, C_{hh}, a_v, b_h, a_{vh}, b_{vh}, a_{hh} and b_{hh} are material coefficients and $f(e)$ is taken as $(2.17\text{-}e)^2/(1+e)$.

Table 2 summarises the cross-anisotropic stiffness coefficients determined from Liu's (2018) study and Kuwano's (1999) earlier Dunkirk sand probing tests. C_h/C_v and C_{hh}/C_{vh}, were invariably greater than unity, indicating inherent anisotropy induced by grain orientation during water (or air) pluviation. Although the simple treatment generally works well, the experiments indicated coefficients that varied moderately with K with C_v values from K = 0.5 tests around 15% above those from K = 1 experiments; see Figure 14.

4.2.2 Non-linear stiffness and yielding

Vinck (2016) and Liu (2018) investigated Dunkirk sand's behaviour from its linear elastic range through to critical state conditions in over sixty locally instrumented tests, varying D_R, effective stress level (p_0') and OCR as well as platen configurations. Figure 15 illustrates the effects of OCR on $E_{v,tan}'/f(e)$ through samples tested at p_0' = 50 and 150 kPa after unloading to a range of OCRs. While over-consolidation affected the initial $E_{v,tan}'$ values by only 5%, it extended the initial linear tangent stiffness plateau through changes in the granular contacts and micro-structure that were accompanied by minimal volume changes and so cannot be captured by, for example, applying a simple *f(e)* function.

Rowe & Barden (1964), Bishop & Green (1965) and Koseki (2021) identified how end friction affects large-strain triaxial behaviour and shear strength of sands. However, its impact on small-strain behaviour was only recently investigated experimentally (with peat) by Muraro & Jommi (2019) and numerically by Cui et al. (2021), considering stiff, high OCR, London clay. Liu et al. (2022a) explored the impact of platen roughness on the pre-failure stiffness of siliceous sand and Figure 16 demonstrates how end constraint affects Dunkirk sand's stiffness and degradation trends even

Table 2. Cross-anisotropy stiffness coefficients of Dunkirk sand.

Sand batch	D_R (%)	Method	K	Stiffness parameters				
Batch 1 (5.85-11.9 m bgl.)	57-65	AP	1, 0.53, 0.35	C_v: 225 a_v: 0.55	C_h: 228 b_h: 0.50	C_{vh}: 70 a_{vh}: 0.36 b_{vh}: 0.20	C_{hh}: 105 a_{hh}: 0.05 b_{hh}: 0.46	C_h/C_v: 1.01 C_{hh}/C_{vh}: 1.5
Batch 3 (0-0.8 m bgl.)	73-92	WP	1, 0.5	C_v: 154 a_v: 0.51	C_h: 166 b_h: 0.50	C_{vh}: 49 a_{vh}: 0.30 b_{vh}: 0.19	C_{hh}: 63 a_{hh}: 0.10 b_{hh}: 0.42	C_h/C_v: 1.08 C_{hh}/C_{vh}: 1.29

Notes: (1) Batch 1 data from Kuwano (1999); (2) Sample preparation method: AP = air pluviation; WP = water pluviation; (3) parameters C_v, C_h, C_{vh} and C_{hv} in MPa; (4) All tests performed with lubricated platens.

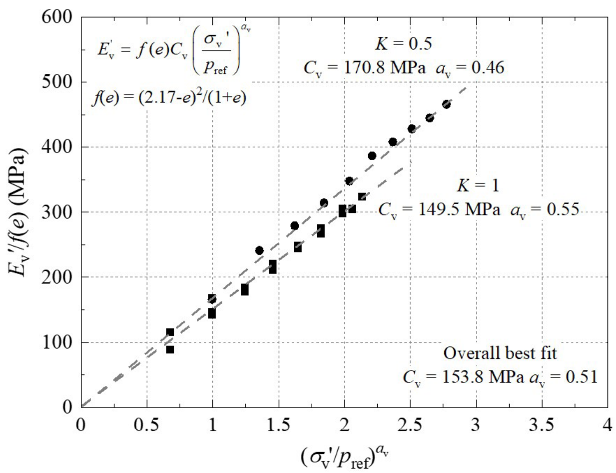

Figure 14. Correlations between $E_v'/f(e)$ and σ_v'/p_{ref} and the stiffness coefficients for the K = 1 and 0.5 small-stress probing tests on Dunkirk sand (Liu, 2018).

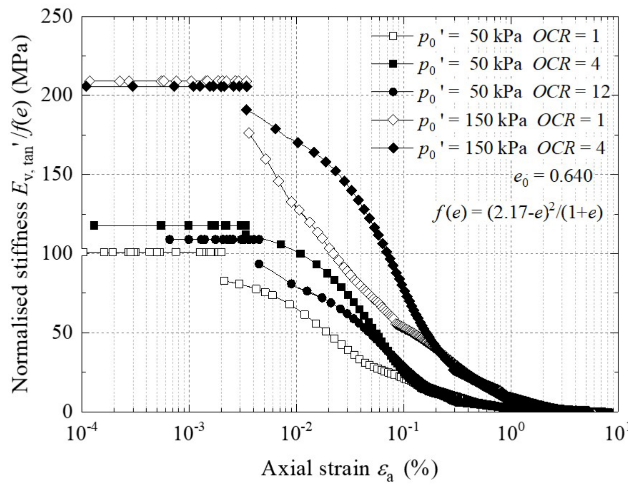

Figure 15. Effects of effective stress level and history on the pre-failure small strain stiffnesses of Dunkirk sand (Liu, 2018).

when specimens had 2:1 initial height-to-diameter ratios and strains were gauged locally over the central ≈ 50 mm height. Figure 16 plots $E_{v,tan}'/f(e)$ against σ_v'/p_{ref} for medium dense specimens, considering axial strains of 0.001%, 0.01%, 0.1% and 1%. Medium density specimens tested at relatively low stress levels were most heavily affected by sample end constraints at low to modest strain levels.

4.2.3 Large-strain and critical state behaviour

End constraint also influences medium-to-large strain behaviour. Full end constraint leads to misleadingly high peak stress ratios and shear strengths, at apparently smaller strains, and ultimate stress ratios that did not tend to converge to a unique M with medium dense specimens. Deformation was more uniform in tests employing enlarged lubricated platens, although bulging about the vertical axis was observed with these specimens, but without visible bifurcation even with very dense specimens.

Liu (2018) interpreted Dunkirk sand's large strain and ultimate shearing behaviour within the state parameter critical state framework, providing the basis for bounding surface plasticity (Taborda et al., 2014) and Nor-Sand (Jefferies & Been, 2015) modelling. Taborda et al. (2020), Castillo-Fuentes et al. (2023) and Selby et al. (2023) demonstrated these models' application in the simulations of the PISA Dunkirk pile tests.

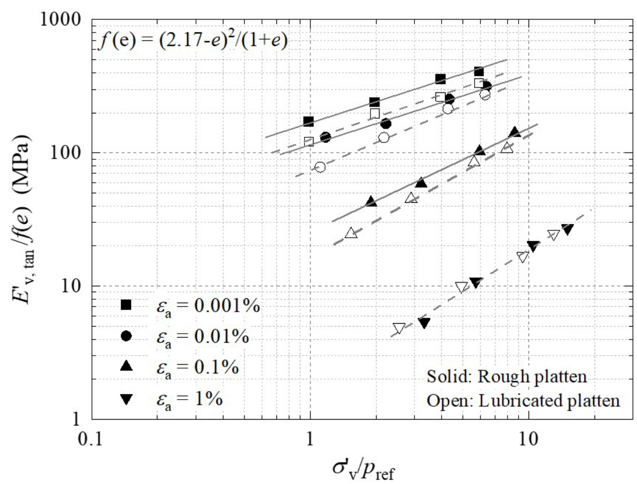

Figure 16. Effects of platen conditions on the pre-failure small strain stiffnesses of medium dense (D_R ≈ 53%) Dunkirk sand specimens (Liu, 2018; Liu et al., 2022a).

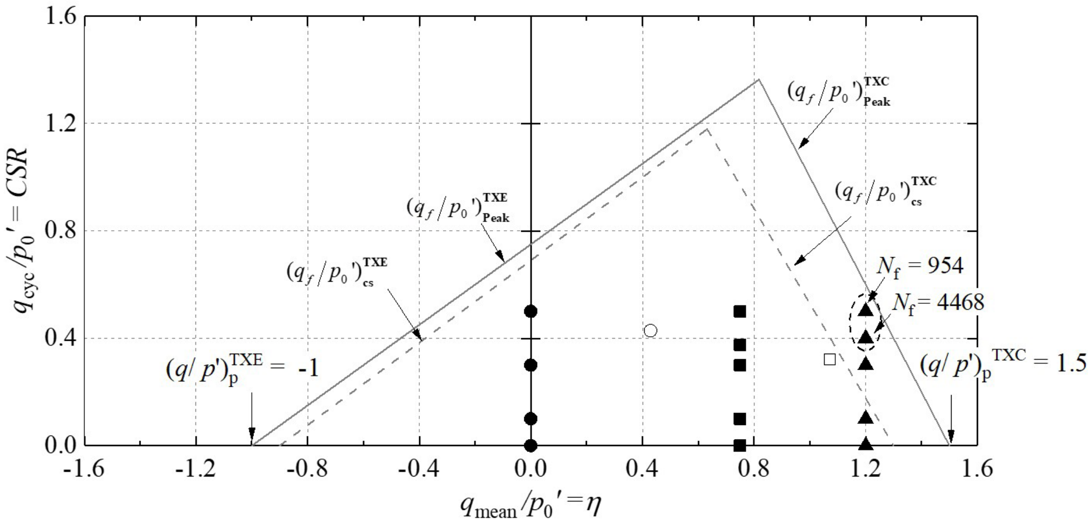

Figure 17. Normalised q_{cyc}/p_0'-q_{mean}/p_0' (CSR-η) stress states with reference to the peak and critical state envelopes of Dunkirk sand (Note $(q/p')_{peak}^{TXC} = 1.5$, $M_{cs}^{TXC} = 1.31$, $(q/p')_{peak}^{TXE} = -1$ and $M_{cs}^{TXE} = -0.9$) (Liu, 2018).

4.3 Long-term drained cyclic loading behaviour

Aghakouchak (2015) and Aghakouchak et al. (2015) conducted cyclic triaxial and hollow cylinder (HCA) tests to model axial cyclic pile loading and showed how to cater for the 'near-shaft' conditions, stress and loading histories that govern field behaviour. Lateral cyclic pile loading engages larger volumes in the passive, active and side shear reaction regions located around the pile circumference. Predominantly drained conditions applied in the PISA Dunkirk tests; conditions are expected to be substantially drained under long-term cyclic loading around even larger monopiles.

Liu's (2018) cyclic triaxial testing programme for Dunkirk therefore focussed on long-term drained constant σ_r' experiments, aiming to produce a benchmark dataset against which cyclic constitutive models could be validated, calibrated, and applied in boundary value problems. The tests applied the cyclic and mean deviatoric stress combinations (q_{cyc}, q_{mean}) as defined in q_{cyc}/p_0'-q_{mean}/p_0' (or CSR-η) space in Figure 17. Specimens were consolidated to, and allowed to creep at, initial (q_{mean}, p_0') states before constant amplitude cycling to target conditions with $N > 10^4$. All but two specimens survived cycling and were subsequently sheared monotonically to failure to assess how cycling had modified their behaviour. Figure 18 illustrates the q–ε_a trends shown for a typical test on a very dense ($D_R = 92\%$) specimen that started from (q_{mean}, p_0') = (100, 133.3) (kPa) with $q_{cyc} = 40$ kPa ($CSR = 0.3$). The local axial strains recorded with high resolution sensors manifested the accumulation trends plotted logarithmically in Figure 19, considering each of the 10^4 cycles. Also annotated are power law equations that fitted the experimental trends. Liu (2018) further related the fitting parameters to the q_{cyc}/p_0'-q_{mean}/p_0' loading conditions and showed how to interpret ratcheting, cyclic stiffness, damping and other cycling characteristics from the high-resolution cycle-by-cycle stress-strain data.

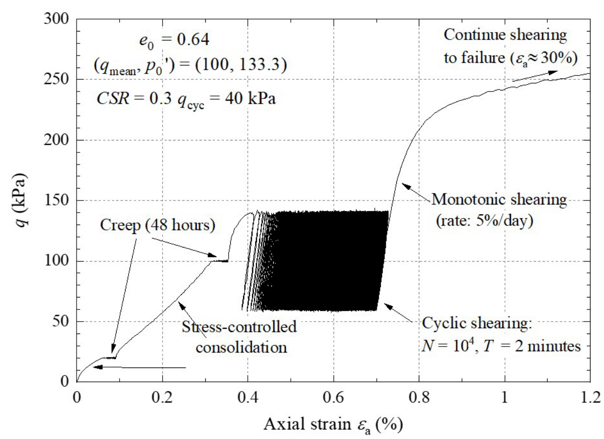

Figure 18. Deviatoric stress strain (q-ε_a) trends for a typical long-term drained cyclic triaxial test involving two sets of stress-controlled consolidation and creep stages, a cyclic shearing stage and post-cyclic monotonic shearing to failure (Liu, 2018).

Post-cyclic shear stiffness trends are considered in Figure 20, plotting normalised secant Young's moduli $E_{v,sec}'$ against axial strain for specimens cycled from the same (q_{mean}, p_0') = (100, 133.3) (kPa) mean conditions but with different amplitudes (q_{cyc}). Applying $f(e)$ accounted for void ratio changes under cycling, showing how cycling led to higher initial stiffness, longer linear plateaux and more gradual stiffness degradation. These changes grew markedly with the prior cyclic stress ratio, reflecting micro-fabric optimisation under cycling. The significantly better organised internal particle force chains and contact distributions also relocated and expanded the sand's Y_1 and Y_2 kinematic yield surfaces.

5. St Nicholas at Wade (SNW) chalk

Extensive laboratory and *in-situ* characterisation were conducted for the ALPACA piling JIP. Noting that pile driving alters chalk properties significantly, the testing considered the behaviour of both intact chalk and the de-structured 'putty' material that formed adjacent to the pile shafts during driving and controlled their axial behaviour. The programme encompassed monotonic and undrained cyclic triaxial loading, supported by geological logging, index, unconfined compression strength (UCS), oedometer, direct simple shear (DSS), Brazilian tension (BT) and interface shear tests (Vinck, 2021). A metallurgical corrosion study was also undertaken by Vinck et al. (2023b) to provide fundamental insights into the piles' highly age-dependent axial shaft capacity trends (Buckley et al., 2018, 2020; Jardine et al., 2023b, c; Vinck et al., 2023a).

5.1 Elastic stiffness profiles

The chalk's elastic stiffnesses were examined by laboratory and field testing and Figure 21 considers the shear stiffness profiles measured at the smallest strains offered by various techniques. As emphasised by Clayton et al. (2003), the chalk's meso-to-macro fabric plays a dominant role. The mean SCPT G_{vh} and cross-hole G_{hv} trends amount to around 2/3 of the shallow triaxial tests' BE G_{vh} measurements and converge more closely at depth, reflecting the reducing occurrence of open fissures, which are naturally excluded from laboratory specimens. The direct simple shear (DSS) G_{vh} maxima and the pressuremeter G_{hh} values fall far below those interpreted from shear wave velocities, due to their low resolution and the chalk's brittle response to the non-uniform straining imposed by these tests. Triaxial BE measurements made on the same samples indicated $G_{hh}/G_{vh} \approx 0.5$ in the shallow layers, which gradually rose to unity at depth; the field seismic data show a similar, but more muted, trend. Also plotted in Figure 21 is the E_h'/E_v' profile developed from four suites of triaxial probing tests by Vinck (2021). Horizontal loading from *in-situ* stresses provokes a far softer response than vertical compression, which is important when analysing lateral pile loading. This aspect of the chalk's marked anisotropy contributed to undrained and drained triaxial compression paths following similarly inclined effective stress paths (Vinck et al., 2022).

5.2 Chalk's response to monotonic triaxial loading

5.2.1 Pressure-dependent yielding and failure

The SNW chalk's cemented open micro-structure (Alvarez-Borges et al., 2020) leads to significant sensitivity, brittleness and pressure-dependent behaviour. Figure 22 shows example loading curves up to 0.5% axial strain from locally instrumented triaxial and UCS tests conducted from in-situ p_0' and 300 kPa + p_0' stresses. Very stiff and nearly linear pre-failure behaviour is evident, as well as a notably brittle post-peak response that involved tensile fracturing and led to low strengths at large strains. High pressure triaxial tests that explored conditions from *in-situ* p_0' ($\approx$ 63 kPa) up to p_0' = 12.8 MPa identified a gradual transition (shown in Figure 23) from brittle to ductile behaviour under increasing p' levels. The chalk's highly curved failure envelope (Figure 24) reaches an ultimate $(q/p')_{ult}$ = 1.25, equivalent to critical state $\phi' \approx 31°$, that matches (as shown later) that of fully de-structured chalk.

Figure 25 depicts how the initial Y_1 and Y_3 yield loci of unfractured chalk may be represented with near elliptical

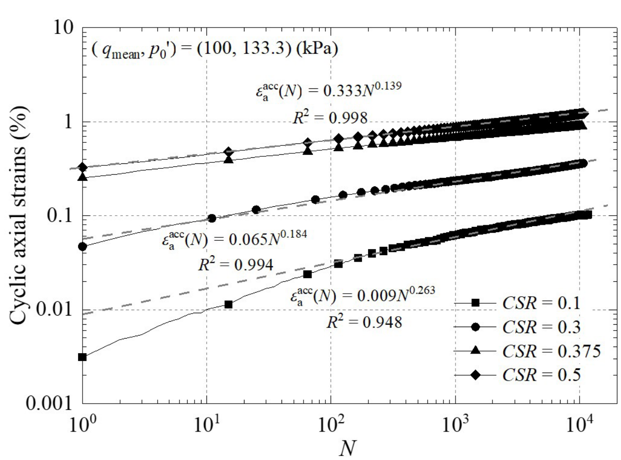

Figure 19. Accumulated cyclic axial strains for very dense (D_R = 92%) triaxial Dunkirk sand specimens cycled from (q_{mean}, p_0') = (100, 133.3) (kPa) under fully drained conditions (Liu, 2018).

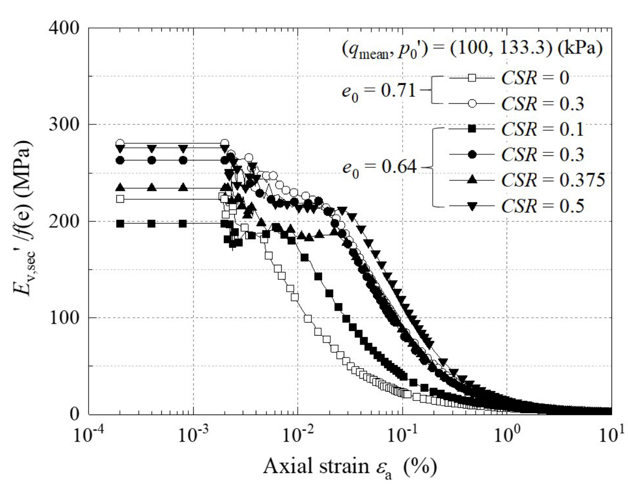

Figure 20. Effects of cyclic loading history on the post-cyclic monotonic stiffness degradation trends for Dunkirk sand (Liu, 2018).

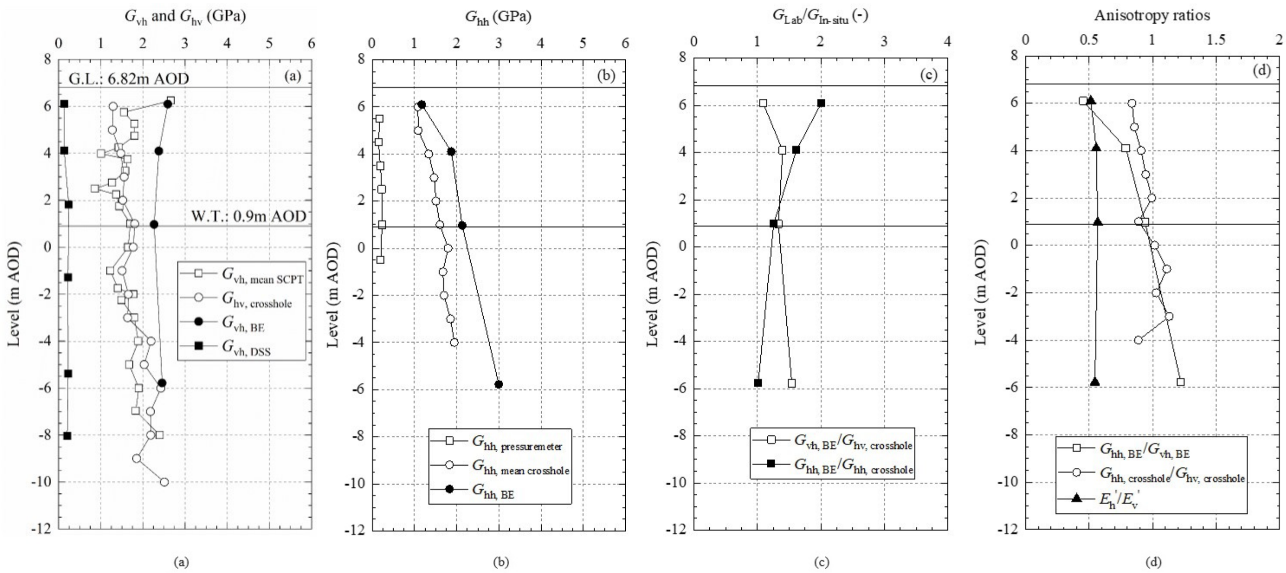

Figure 21. SNW profiles and ratios of maximum stiffnesses: (a) laboratory and in-situ measurements of G_{vh} and G_{hv}; (b) G_{hh} profiles; (c) ratios between laboratory and in-situ stiffnesses; and (d) profiles of stiffness anisotropy ratios (modified from Vinck et al., 2022).

surfaces in triaxial q-p' space. Intact (cemented) chalk displays linear behaviour over a far larger region of q-p' space than soils such as the unbonded Cowden till or Dunkirk sand. Laboratory elastic vertical Young's moduli $E_{v,max}'$ are comparatively insensitive to applied p_0', with modest increases up to the peak (7.7 GPa) found with p_0' = 650 kPa before falling to a 4 MPa plateau as bonds break under increasing p_0' (Liu et al., 2023b). However, the chalk's systems of micro-to-macro fissures, which gradually close under normal stress, lead to the maximum mass chalk stiffnesses invoked by pile loading being four times lower than the laboratory values (Jardine et al., 2023c).

Chalk's propensity to tensile fracture leads to BT and DSS strengths 90% and 50% lower respectively than those from UCS or triaxial compression tests, with many implications for the modelling of geotechnical problems that involve multi-directional loading.

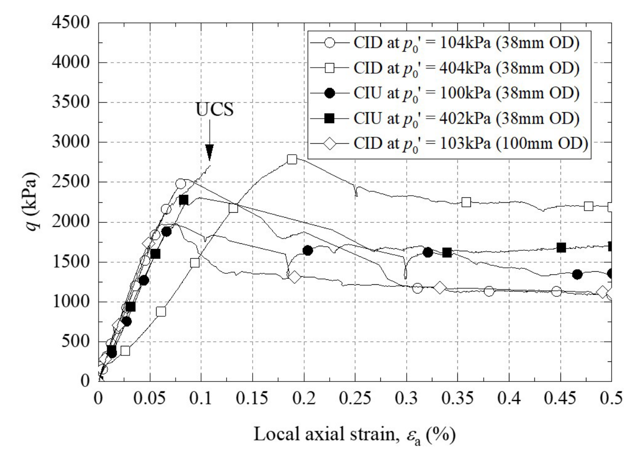

Figure 22. Example stress-strain curves up to 0.5% axial strain from locally instrumented triaxial and unconfined compression (UCS) tests on intact SNW chalk from in-situ p_0' and 300 kPa + p_0' (Vinck et al., 2022).

5.2.2 Fully de-structured chalk's response to undrained monotonic shearing

Laboratory dynamic compaction, applied at in-situ water content, was employed to de-structure low-to-medium density chalk in an analogous way to pile driving, producing uniform chalk putty with 9 ± 3 kPa fall-cone shear strengths and liquid and plastic limits of 30.6% and 24.2% respectively. Instrumented, consolidated, triaxial specimens were formed with (pre-shearing) void ratios and effective stress states matching those noted in the de-structured annuli identified around driven pile shafts several months after driving (Buckley et al., 2018).

The de-structured chalk's undrained triaxial compression and extension behaviour is demonstrated first in Figure 26 by considering the q-p' effective stress paths. These are initially nearly vertical, suggesting that the re-consolidated and (mildly aged) putty's initial stiffness response was largely isotropic. The effective stress paths rotated to follow leftward (contractive) stages after mobilising modest 'peak' resistances (at ε_a < 0.2%) and showed strain softening as shearing continued up to phase transformation (PT) points at which their paths rotated abruptly and climbed towards ultimate (critical state) conditions. Continued straining led to markedly higher ultimate strengths as the specimens attempted to continue dilating. Extension tests indicated similar, yet not fully symmetric, paths and shear strengths.

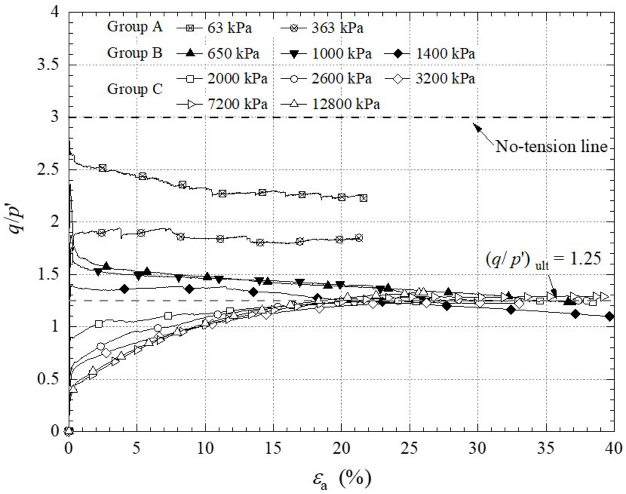

Figure 23. Full-strain triaxial compression behaviour of intact SNW chalk under a wide range of pressures (Liu et al., 2023b).

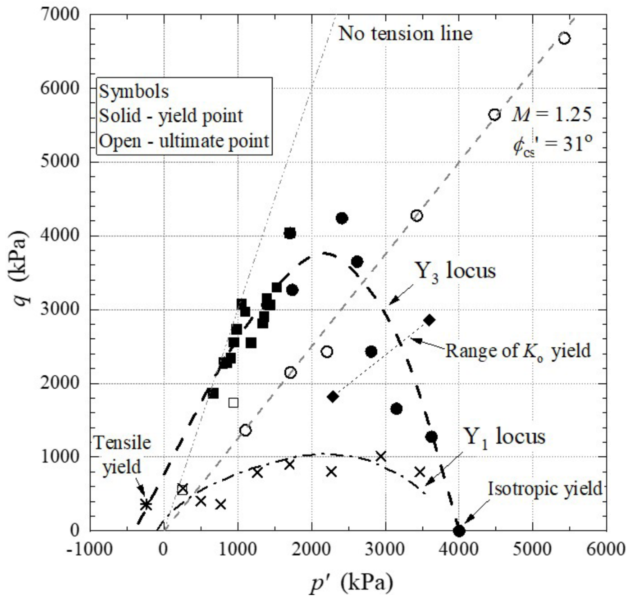

Figure 25. Yield stresses and interpreted pre-failure Y_1 and large-scale Y_3 loci for intact SNW chalk (Liu et al., 2023b).

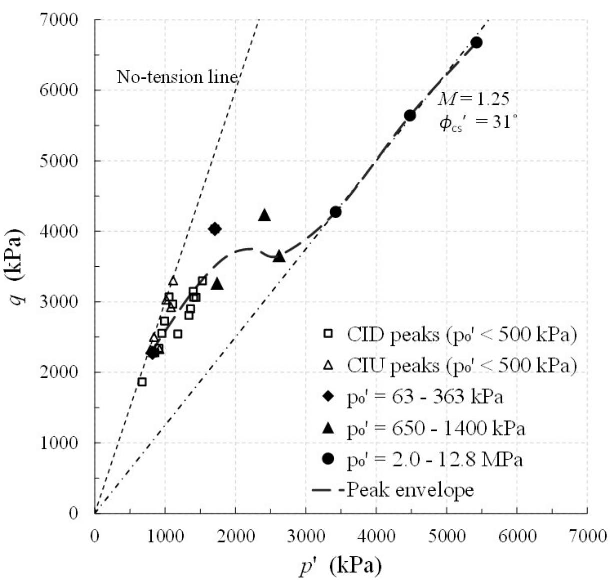

Figure 24. Peak and ultimate shear strength envelope for intact SNW chalk (Liu et al., 2023b).

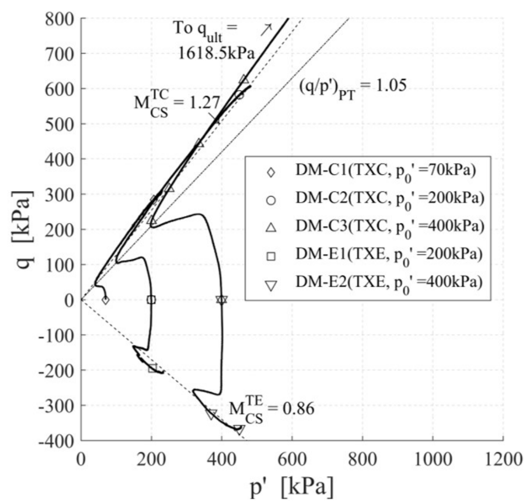

Figure 26. Effective stress paths of de-structured chalk under undrained triaxial compression and extension (modified from Liu et al., 2022b).

The ultimate critical states gave $\phi_{cs}' \approx 31°$, matching the high-pressure intact tests in Figure 24.

5.3 Response to undrained cyclic triaxial loading

5.3.1 Intact chalk's failure patterns

Undrained cycling affects intact chalk differently to saturated sedimentary sands or clays (Ahmadi-Naghadeh et al., 2022). Figure 27 presents a typical unstable response observed with a specimen loaded from $p_0' = 42$ kPa, $q_{mean} = 1225$ kPa by high-level cycling with $q_{cyc} = 950$ kPa and $q_{max}/(2S_u) = 0.91$. The axial strain and pore pressure records show little or no sign of impending instability; little change was seen in either the damping ratio (which remained at around 4%) or the cyclic stiffness, until degradation set in over the last 30 cycles and brittle failure occurred abruptly after 181 cycles. In contrast, specimens that sustained large number (> 4,000) of cycles developed minimal straining and excess pore pressure accumulation and manifested nearly visco-elastic behaviour.

The experimental outcomes allow cyclic interaction diagrams to be established in $q_{cyc}/(2S_u)$–$q_{mean}/(2S_u)$ space, as in Figure 28. A tentative fan of linear N_f contours indicates the

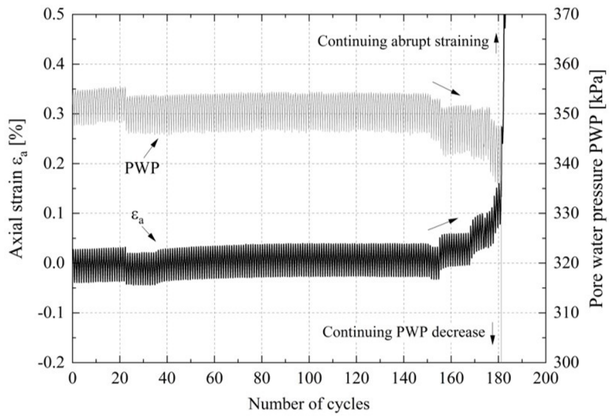

Figure 27. Typical unstable cycling response of intact chalk: Variation of axial strain and pore water pressure against number of cycles (Test conditions: p_0' = 42 kPa, q_{mean} = 1225 kPa, q_{cyc} = 950 kPa and $q_{max}/(2S_u)$ = 0.91) (Ahmadi-Naghadeh et al., 2022).

main trends applying between 1 and 3000 cycles. The region below the 3000-cycle contour in Figure 28 signifies the stable region within which undrained cycling improved stiffness without any loss of undrained shear strength.

Overall, the intact chalk's behaviour appears more like that of crystalline rocks or metals than sedimentary soils. Repeated loading prompts progressive wear and shearing between grains, forming microcracks that may coalesce into macrocracks (Cerfontaine & Collin, 2018). The outcomes can be interpreted as 'S-N' curves that plot the maximum cyclic load ($q_{max} = q_{mean} + q_{cyc}$) against log N, with contours interpolated to show how the $q_{max}/(2S_u)$ curves fall as q_{cyc}/q_{mean} rises, expressed as:

$$\frac{q_{\max}}{2S_{\mathrm{u}}} = f(N)\cdot\frac{1+q_{\mathrm{cyc}}/q_{\mathrm{mean}}}{f(N)+q_{\mathrm{cyc}}/q_{\mathrm{mean}}} \tag{6}$$

in which $f(N)$ represents for each N_f line its projected intercept on the vertical axis of the interactive $q_{cyc}/(2S_u)$-$q_{mean}/(2S_u)$ diagram and is expressed as:

$$f(N) = 0.35 + \frac{1}{1.54 + 0.37\times[\log_{10}(N_{\mathrm{f}})]^{2.75}} \tag{7}$$

A lower limit of $f(N)$ = 0.35 is incorporated in this expression which corresponds to a fatigue limit (or fatigue strength) of $q_{max}/(2S_u)$ = 0.52, below which specimens could sustain cycles indefinitely under the most critical q_{cyc}/q_{mean} = 1 one-way loading condition. The above two equations lead further to a three-dimensional representation of intact chalk's undrained cyclic failure characteristics in a $q_{max}/(2S_u)$-q_{cyc}/q_{mean}-$\log_{10}(N)$ space, as shown in Figure 29.

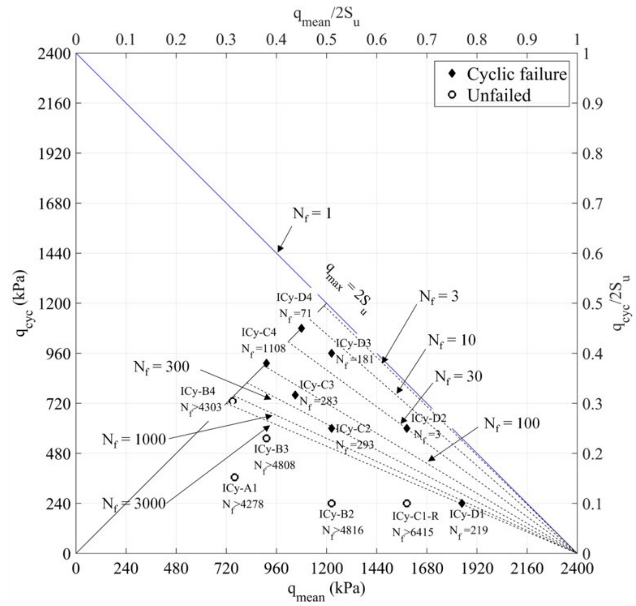

Figure 28. Cyclic interaction diagram for intact SNW chalk tested from p_0' = 42 kPa, showing the interpreted contours of number of cycles to failure for specified q_{cyc}-q_{mean} conditions (Ahmadi-Naghadeh et al., 2022).

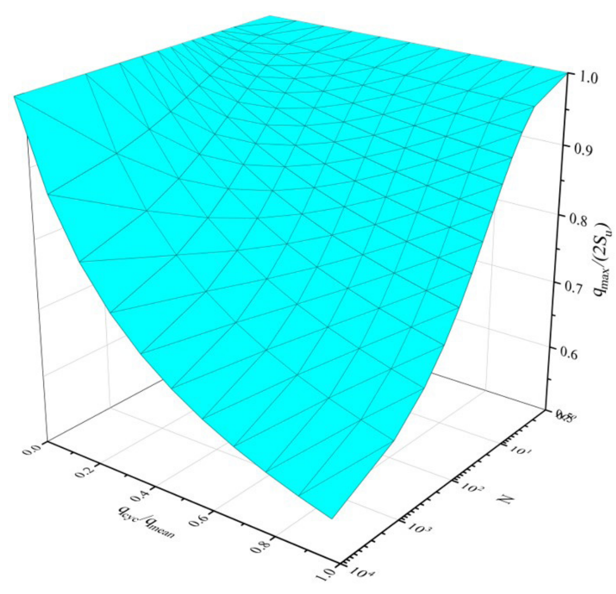

Figure 29. Three-dimensional representation of the undrained cyclic failure characteristics of intact SNW chalk in $q_{max}/(2S_u)$-q_{cyc}/q_{mean}-$\log_{10}(N)$ space (Ahmadi-Naghadeh et al., 2022).

5.3.2 Cyclic failure characteristics of de-structured chalk

Liu et al. (2022b) show that fully de-structured, re-consolidated, chalk putty responds to undrained cyclic loading similarly to silts and silty sands, and markedly differently to the intact chalk. As illustrated in Figure 30, de-structured specimens respond to high-level cycling by generating excess pore pressures that shift their effective stress paths leftwards. Both contractive and dilative phases occur within individual cycles. Cyclic phase transformation lines with (q/p') gradients of ≈ 0.54 and 0.38 can be identified in compression and extension respectively, following Mao & Fahey (2003), that fall well below the monotonic phase transformation lines. The transient cyclic effective stress paths can also cross the monotonic critical state gradients M.

The full suite of one- and two-way cyclic tests is set-out in an interactive loading diagram in Figure 31, which adopts both $q_{cyc}/(2S_u)$-$q_{mean}/(2S_u)$ and $q_{cyc}/(p_0')$-$q_{mean}/(p_0')$ axes. A tentative family of contours is shown for number of cycles to failure (N_f); the lower-levels, high N_f, contours show less curvature and tighter spacings than those representing high-level cycling. As with all soils, chalk putty is more susceptible to high-level two-way (compression and extension, with $q_{mean} \leq q_{cyc}$) loading than one-way compression cycling.

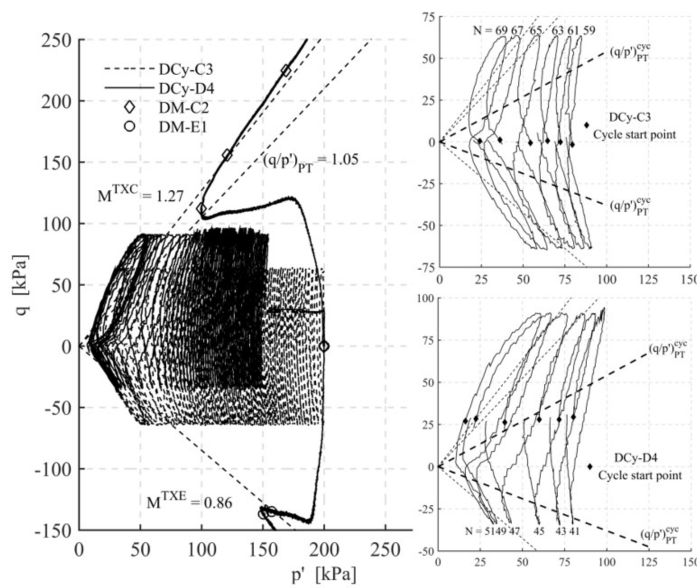

Figure 30. Effective stress paths for typical unstable tests on de-structured chalk and the identified cyclic phase transformation lines (Liu et al., 2022b).

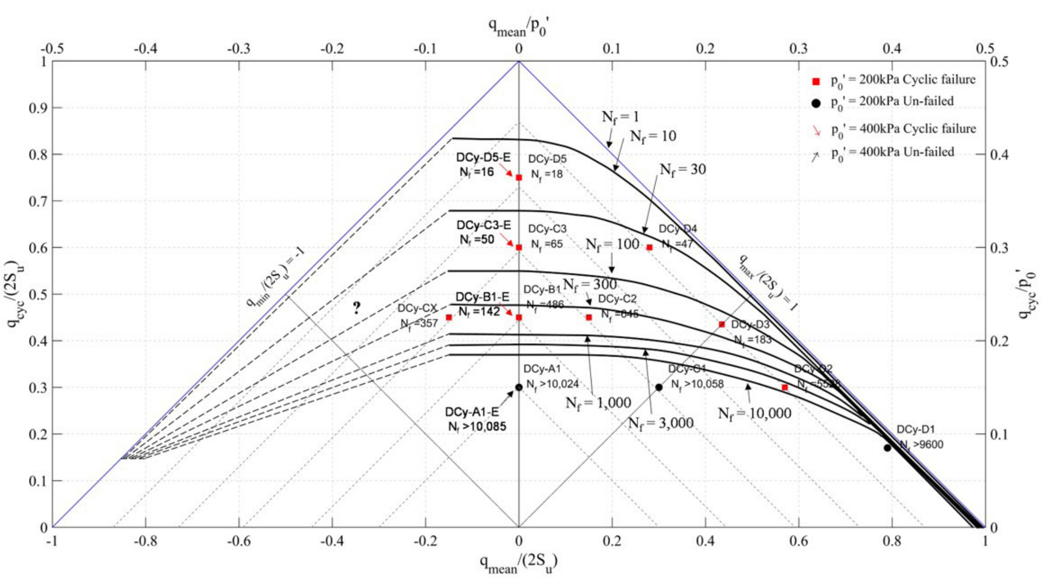

Figure 31. Cyclic interaction diagram for de-structured chalk expressed in normalised $q_{cyc}/(2S_u)$ - $q_{mean}/(2S_u)$ and q_{cyc}/p_0' - q_{mean}/p_0' stress space for p_0' = 200 kPa and p_0' = 400 kPa test series (Liu et al., 2022b).

Significant axial strain development and stiffness losses occur in unstable tests that accelerate markedly as cyclic failure approaches. Liu et al. (2022b) report on these features and the specimens' damping ratios. Cycle-by-cycle effective stress changes were tracked in the experiments, enabling the development of a laboratory-based global prediction method for axial shaft capacity under cyclic loading (Jardine, 2020; Buckley et al., 2023). All tests showed $\Delta p'/p_0'$ decreasing continuously with N, although it is possible that cycling at lower levels than those applied would identify conditions under which no reduction occurs. Liu et al. (2022b) show that the mean effective stress drifts of tests run with $(q_{cyc}+q_{mean})/p_0' < 0.4$ can be related to the number of cycles applied by the power-law Equation 8.

$$\frac{p'}{p_0'} = A\times(B+\frac{q_{\mathrm{cyc}}}{p_0'})\times N^C \tag{8}$$

Parameters A, B and C define the rates of p' degradation and the maximum cyclic stress ratio that could lead to beneficial, null, or deleterious cycling effects. Higher level cyclic tests that failed within just a few cycles show more complex trends. Figure 32 reports the outcomes of cyclic tests on samples consolidated to $p_0' = 200$ kPa and shows how Equation 8, applied with $A = -0.05$ and $B = -0.12$ and $C = 3.48\times q_{cyc}/p_0'$ fits the experimental trends well.

6. Applications of the research

The Cowden, Dunkirk and SNW characterisation programmes were vital to interpretating the high-value, large-scale, instrumented pile experiments run at the three sites. They also led to new site investigation and practical pile design approaches that are being applied widely in major offshore wind projects. As noted below, advances have flowed in four main areas.

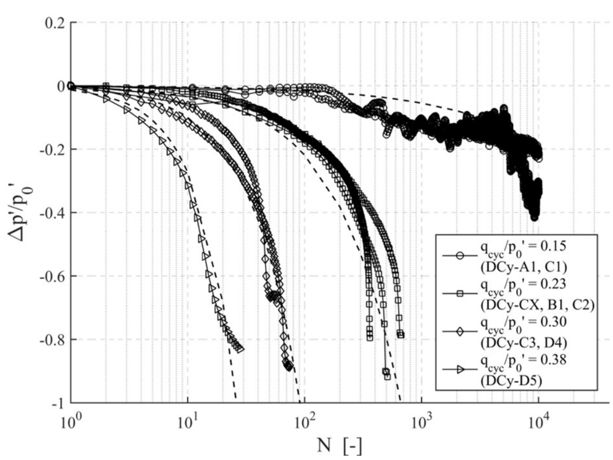

Figure 32. Mean effective stress trends during cycling and fitted trends (in dashed lines) for 'putty' tests with $p_0' = 200$ kPa and mostly $(q_{cyc}+q_{mean})/p_0' < 0.4$ (Liu et al., 2022b).

6.1 Pile behaviour under monotonic axial loading

Jardine et al. (2005) and Jardine (2014) showed that advanced finite element (FE) modelling based on the glacial tests by Jardine et al. (1984) and sand tests by Kuwano (1999) offered good matches to full-scale field observations made at North Sea clay till sites and tests to failure on 19 m long, 457 mm diameter piles driven at Dunkirk. The most significant new findings to emerge regarding axial load-displacement behaviour, which is central to jacket supported structures, therefore concern the chalk, about which little information was available previously. Wen et al. (2023a, b) employed the laboratory testing to calibrate new 1D load transfer and advanced 2D/3D FE models that provide generally good fits to the ALPACA and ALPACA Plus field tests on piles with diameters up to 1.8 m and embedded lengths up to 18 m.

6.2 Pile behaviour under cyclic axial loading

Buckley et al. (2023) and Liu et al. (2023c) report on how the laboratory chalk putty cyclic testing contributed to a simplified yet accurate global prediction method for axial cyclic pile design in chalk, which is now available for use by industry. Jardine (2020) and Jardine et al. (2012) have reported previously on the use of undrained cyclic tests on sands and clays to predict pile response to axial loading, showing how the laboratory experiments by Aghakouchak et al. (2015) on Dunkirk sand enabled accurate predictions of the cyclic axial pile tests reported by Jardine & Standing (2012). The Cowden till cyclic testing data is also now available to aid back-analysis of earlier cyclic axial pile tests (see Ove Arup and Partners, 1988) as well as monotonic axial tests reported by Karlsrud et al. (2014).

6.3 Pile behaviour under monotonic lateral loading

Modelling of field lateral pile loading response is critical to the efficient design of monopile supported offshore wind turbines. Taborda et al. (2020) and Zdravković et al. (2020b) describe how the site characterisation described above was central to advanced 3D FE analyses that aided the design and interpretation of the PISA lateral loading tests on instrumented piles with diameters up to 2 m driven at Dunkirk and Cowden. The resulting PISA design approach (Byrne et al., 2020c) has offered a step change in design practice that has been applied internationally. Pedone et al. (2023) describe how still more advanced 3D FE analyses developed from the chalk testing captured accurately the lateral loading behaviour shown by ALPACA tests in the fractured, highly brittle SNW chalk. These experiments and analyses are now being applied in the design of major new windfarms at offshore chalk sites.

6.4 Pile behaviour under cyclic lateral loading

It is essential to consider lateral cyclic loading cases when designing monopile foundations. The PISA cyclic pile tests are applied widely as benchmarks against which alternative modelling strategies are routinely calibrated and tested. The Authors' recently published cyclic laboratory test programmes offer a basis for re-analyses of the Cowden and Dunkirk cyclic PISA pile tests, as well as the recent PICASO tests (Byrne et al., 2020a) at Cowden. The cyclic laboratory programmes on chalk will also pave the way for well-calibrated lateral cyclic analyses at chalk sites.

7. Summary and conclusions

This paper summarises recent research into the stiff glacial till, dense marine sand, and low-to-medium density chalk encountered at the PISA, ALPACA and ALPACA Plus JIPs instrumented pile test sites. Coordinated field and laboratory studies investigated the materials' stiffness patterns, full strain mechanical behaviour, anisotropy and response to cyclic loading. Their outcomes are being employed widely to aid the modelling of field behaviour under axial-and-lateral, monotonic-and-cyclic loading. By enabling more efficient driven pile foundation design, the research is contributing significantly to more efficient offshore wind energy generation and CO_2 emission reductions. The large volume of new findings supports four general conclusions.

1. Monotonic laboratory testing to failure showed how the geomaterials behave over their full strain range, including the distinct properties of the fully de-structured chalk putty. Combining these data with *in-situ* measurements enables representative modelling of the pile test outcomes and shows the way forward for their practical application;
2. Laboratory and field measured elastic stiffnesses may show significant divergence. While broadly similar profiles applied at Cowden, triaxial tests on reconstituted Dunkirk sand underpredicted the site's field stiffnesses, which had grown after 20 years of ageing under hydraulic fill. In contrast, the chalk's mass field stiffness fell far below the measurements made from laboratory tests on intact samples because they did not capture the important effects of partially open meso-to-macro fractures;
3. All three geomaterials displayed elastic stiffness anisotropy. Vertical stiffnesses exceeded horizonal moduli in the normally consolidated dense Dunkirk sand and in the high YSR intact SNW chalk, while the opposite applied in high YSR Cowden glacial till;
4. The cyclic programmes showed a wide range of behaviours and provide vital new evidence to aid the development of suitable predictive approaches. While the intact chalk's response was distinctly different to that of the till and sand, resembling that of crystalline rocks or metals, the chalk putty's cyclic behaviour was closer to that shown by the glacial till and marine sand.

Acknowledgements

The first author is deeply grateful to Lidija Zdravković, Erdin Ibraim and Andrea Diambra who provided essential guidance for writing up this paper and lecture. Parts of the laboratory testing campaigns on Cowden till and Dunkirk sand were undertaken to support the PISA JIP project managed by Ørsted. The PISA sponsors' and Academic Working Group's support is acknowledged thankfully, as is the financial support provided by Ørsted for the later Post-PISA Experimental Project. The studies on St Nicholas at Wade (SNW) chalk were undertaken as part of the ALPACA project funded by the Engineering and Physical Science Research Council (EPSRC) grant EP/P033091/1 and Royal Society Newton Advanced Fellowship NA160438. The authors acknowledge gratefully additional financial and technical support from Atkins, Cathie Associates, Equinor, Fugro, Geotechnical Consulting Group (GCG), Iberdrola, Innogy, LEMS, Ørsted, Parkwind, Siemens, TATA Steel and Vattenfall. Ken Vinck acknowledges Imperial College's EPSRC Centre for Doctoral Training (CDT) in Sustainable Civil Engineering and the DEME Group (Belgium) for supporting his doctoral research. The kind support and contributions of many collaborators are acknowledged gratefully including those of Amin Aghakouchak, Reza Ahmadi-Naghadeh, Amandine Brosse, Róisín Buckley, Byron Byrne, Matteo Ciantia, Matthew Coop, Wenjie Cui, Pedro Ferreira, Stavroula Kontoe, James Lawrence, Ross McAdam, Satoshi Nishimura, Catherine O'Sullivan, Giuseppe Pedone, David Potts, David Taborda, Kai Wen, Hongjie Zhou and others. Invaluable technical support by Steve Ackerley, Graham Keefe, Prash Hirani, Stef Karapanagiotidis, Graham Nash and Gary Jones is acknowledged gratefully. Finally, the authors thank their families for their patient and essential support, which was crucial to enabling the presented research.

Declaration of interest

The authors have no conflicts of interest to declare. All co-authors have observed and affirmed the contents of the paper and there is no financial interest to report.

Authors' contributions

Tingfa Liu: conceptualization, investigation, data curation, methodology, formal analysis, writing – original draft. Ken Vinck: conceptualization, investigation, data curation, methodology, formal analysis, writing – review & editing. Emil R. Ushev: conceptualization, investigation, data curation, methodology, formal analysis, writing – review & editing. Richard J. Jardine: supervision, methodology, project administration, funding acquisition, writing – review & editing.

Data availability

Some data that support the findings of this study are available from the corresponding author upon reasonable request.

List of symbols and abbreviations

a_v, a_{vh}, a_{hh}	Cross-anisotropy stiffness parameters; see Equations 2-5
b	Intermediate principal stress factor (= $(\sigma_2 - \sigma_3)/(\sigma_1 - \sigma_3)$)
b_h, b_{vh}, b_{hh}	Cross-anisotropy stiffness parameters; see Equations 2-5
c'	Soil cohesion
e	Void ratio
e_0	Specimen initial void ratio
p'	Mean effective stress
$p'_{in\text{-}situ}$	*In-situ* mean effective stress
p_0'	Initial mean effective stress
p_{ref}	Reference atmospheric pressure (= 101.3 kPa)
q	Deviatoric stress
q_c, q_t	Measured cone resistance and cone resistance corrected for pore pressure respectively
q_{cyc}	Cyclic deviatoric stress amplitude (= $(q_{peak} - q_{trough})/2$)
q_f	Deviatoric stress at failure
q_{mean}	Mean q applied in stress cycle
q_{max}	Maximum q applied in stress cycle (= $q_{mean} + q_{cyc}$)
q_{trough}	Minimum q applied in stress cycle (= $q_{mean} - q_{cyc}$)
q_{PT}	Deviatoric stress at the phase transformation state
wc	Water content
w_L	Liquid limit
w_p	Plasticity limit
ALPACA	Axial-Lateral Pile Analysis for Chalk Applying multi-scale field and laboratory testing
AOD	Above ordnance datum
BE	Bender element test
CPTu	Cone penetration test with pore pressure measurement
CSR	Cyclic stress ratio (= q_{cyc}/p_0')
C_v, C_h, C_{vh}, C_{hh}	Cross-anisotropy stiffness parameters, see Equations 2-5
D_R	Relative density
DSS	Direct simple shear
D_{50}	Mean particle diameter
E_v', E_h'	Drained vertical and horizontal Young's moduli respectively
E_v^u, E_h^u	Undrained vertical and horizontal Young's moduli respectively
E_u^{TXC}	Undrained Young's modulus determined from triaxial compression tests
E_{sec}^u	Undrained secant Young's modulus
G_{hh}	Shear modulus in horizontal plane
G_{hv},G_{vh}	Shear modulus in vertical plane
$G_{z\theta}$	(= G_{vh}) Shear modulus in vertical plane
G_0	Elastic shear stiffness
G_{oct}	Octahedral shear modulus
G_s	Specific gravity
HCA	Hollow Cylinder Apparatus
IDD	Intact dry density
JIP	Joint industry project
KUC	K_o-consolidated undrained compression
KUE	K_o-consolidated undrained extension
K_0	Coefficient of earth pressure at rest
LVDT	Linear variable differential transformer
M	Critical state q/p' stress ratio
M_{cs}^{TXC}, M_{cs}^{TXE}	Critical state stress ratio under triaxial compression and extension
N	Number of cycles
N_f	Number of cycles to failure
N_{kt}	Cone factor defined as $N_{kt} = (q_t - \sigma_{v0})/S_u$
OCR	Over-consolidation ratio
PI	Plasticity index
PISA	PIle Soil Analysis
PT	Phase transformation
SCPT	Seismic cone penetration test
S_r	Saturation degree
S_u	Undrained shear strength
S_u^{TXC}, S_u^{TXE}	Undrained shear strength under triaxial compression and extension
TXC, TXE	Triaxial compression and extension respectively
YSR	Yield stress ratio
α	Angle between the vertical and the direction of σ_1 axis
$\alpha_{d\sigma}$	Angle between the vertical and the direction of $\Delta\sigma_1$ axis
α_f	Angle between the vertical and the direction of σ_1 axis at ultimate failure
$\gamma_{z\theta}$	Torsional shear strain
Δu	Excess pore water pressure
δ_{ult}'	Ultimate soil-structure interface shear resistance angle
ε_a, ε_v	Axial (vertical) strain
ε_{mean}	Permanent axial strain accumulated in cyclic tests
ε_r	Radial (horizontal) strain

ε_s	Shear strain (= ε_a for undrained triaxial condition)
ε_z, ε_r, ε_θ	Axial, radial and circumferential strains respectively in HCA space
ε_v, ε_h	Vertical (axial) and horizontal (radial) strains respectively in triaxial space
ε_1, ε_3	Major and minor principal strain respectively
η	Mean stress ratio (= q_{mean}/p_0')
ρ_{bulk}	Bulk density
σ_1, σ_2, σ_3	Major, intermediate and minor principal stresses respectively
σ_v', σ_h'	Vertical and horizontal effective stress respectively
σ_{vy}'	One-dimensional (1-D) compression yield stress
σ_{v0}'	In-situ vertical effective stress
$\tau_{z\theta}$	Torsional shear stress
ϕ'	Effective angle of shearing resistance
ϕ'_{cs}	Critical state shear resistance angle
ϕ'_{peak}	Shear resistance angle at peak

References

Aghakouchak, A. (2015). *Advanced laboratory studies to explore the axial cyclic behaviour of driven piles* [Doctoral thesis]. Department of Civil and Environmental Engineering, Imperial College London, London, UK. Retrieved in August 23, 2023, from https://spiral.imperial.ac.uk/handle/10044/1/28900

Aghakouchak, A., Sim, W.W., & Jardine, R.J. (2015). Stress-path laboratory tests to characterise the cyclic behaviour of piles driven in sands. *Soil and Foundation*, 55(5), 917-928. http://doi.org/10.1016/j.sandf.2015.08.001.

Ahmadi-Naghadeh, R., Liu, T., Vinck, K., Jardine, R.J., Kontoe, S., Byrne, B.W., & McAdam, R.A. (2022). A laboratory characterization of the response of intact chalk to cyclic loading. *Géotechnique*, 1-13. http://doi.org/10.1680/jgeot.21.00198.

Alvarez-Borges, F., Madhusudhan, B.N., & Richards, D. (2020). Mechanical behaviour of low-medium density destructured White Chalk. *Géotechnique Letters*, 10(2), 360-366. http://doi.org/10.1680/jgele.20.00009.

Bishop, A.W., & Green, G.E. (1965). The influence of end restraint on the compression strength of a cohesionless soil. *Géotechnique*, 15(3), 243-266. http://doi.org/10.1680/geot.1965.15.3.243.

Brosse, A.M., Hosseini Kamal, R., Jardine, R.J., & Coop, M.R. (2017). The shear stiffness characteristics of four Eocene-to-Jurassic UK stiff clays. *Géotechnique*, 67(3), 242-259. http://doi.org/10.1680/jgeot.15.P.236.

Brucy, F., Meunier, J., & Nauroy, J.F. (1991). Behaviour of pile plug in sandy soils during and after driving. In *Proceedings of the 23rd Offshore Technology Conference* (pp. 145-154), Houston, TX, USA. http://doi.org/10.4043/6514-MS.

Buckley, R.M. (2018). *The axial behaviour of displacement piles in chalk* [Doctoral thesis]. Imperial College London, London, UK. Retrieved in August 23, 2023, from https://spiral.imperial.ac.uk/handle/10044/1/78617

Buckley, R.M., Jardine, R.J., Kontoe, S., Parker, D., & Schroeder, F.C. (2018). Ageing and cyclic behaviour of axially loaded piles driven in chalk. *Géotechnique*, 68(2), 146-161. http://doi.org/10.1680/jgeot.17.P.012.

Buckley, R.M., Jardine, R.J., Kontoe, S., Barbosa, P., & Schroeder, F.C. (2020). Full-scale observations of dynamic and static axial responses of offshore piles driven in chalk and tills. *Géotechnique*, 70(8), 657-681. http://doi.org/10.1680/jgeot.19.TI.001.

Buckley, R.M., Jardine, R.J., Kontoe, S., Liu, T., Byrne, B.W., McAdam, R.A., Schranz, F., & Vinck, K. (2023). Axial cyclic loading of piles in low to medium density chalk. *Géotechnique*, 1-14. In press. http://doi.org/10.1680/jgeot.22.00044.

Byrne, B.W., McAdam, R.A., Burd, H.J., Houlsby, G.T., Martin, C.M., Beuckelaers, W.J.A.P., Zdravkovic, L., Taborda, D.M.G., Potts, D.M., Jardine, R.J., Ushev, E., Liu, T., Abadias, D., Gavin, K., Igoe, D., Doherty, P., Gretlund, J., Andrade, M.P., Wood, A.M., Schroeder, F.C., Turner, S., & Plummer, M.A.L. (2017). PISA: new design methods for offshore wind turbine monopiles. In *Proceedings of the 8th International Conference on Offshore Site Investigation and Geotechnics* (pp. 142-161), London. http://doi.org/10.3723/OSIG17.142

Byrne, B.W., Aghakouchak, A., Buckley, R.M., Burd, H.J., Gengenbach, J., Houlsby, G.T., Mc Adam, R.A., Martin, C.M., Schranz, F., Sheil, B.B., & Suryasentana, S.K. (2020a). PICASO: cyclic lateral loading of offshore wind turbine monopiles. In *Proceedings of the 4th International Symposium Frontiers in Offshore Geotechnics*, Austin, Texas.

Byrne, B.W., McAdam, R.A., Burd, H.J., Beuckelaers, W.J., Gavin, K.G., Houlsby, G.T., Igoe, D.J., Jardine, R.J., Martin, C.M., Muir Wood, A., Potts, D.M., Skov Gretlund, J., Taborda, D.M.G., & Zdravković, L. (2020b). Monotonic laterally loaded pile testing in a stiff glacial clay till at Cowden. *Géotechnique*, 70(11), 970-985. http://doi.org/10.1680/jgeot.18.PISA.003.

Byrne, B.W., Houlsby, G.T., Burd, H.J., Gavin, K.G., Igoe, D.J., Jardine, R.J., Martin, C.M., McAdam, R.A., Potts, D.M., Taborda, D.M.G., & Zdravković, L. (2020c). PISA design model for monopiles for offshore wind turbines: application to a stiff glacial clay till. *Géotechnique*, 70(11), 1030-1047. http://doi.org/10.1680/jgeot.18.P.255.

Castillo-Fuentes, E., Zdravković, L., & Potts, D.M. (2023). On the calibration and application of the NorSand model. In L. Zdravković, S. Kontoe, D.M.G. Taborda, & A. Tsiampousi (Eds.), *Proceedings of the 10th European Conference on Numerical Methods in Geotechnical Engineering*, London, UK. http://doi.org/10.53243/NUMGE2023-242.

Cerfontaine, B., & Collin, F. (2018). Cyclic and fatigue behaviour of rock materials: review, interpretation and research perspectives. *Rock Mechanics and Rock Engineering*, 51(2), 391-414. http://doi.org/10.1007/s00603-017-1337-5.

Chow, F. (1997). *Investigations into the behaviour of displacement piles for offshore foundations* [Doctoral thesis]. Imperial College, University of London, London, UK. Retrieved in August 23, 2023, from https://spiral.imperial.ac.uk/handle/10044/1/7894

Ciavaglia, F., Carey, J., & Diambra, A. (2017). Time-dependent uplift capacity of driven piles in low to medium density chalk. *Géotechnique Letters*, 7(1), 90-96. http://doi.org/10.1680/jgele.16.00162.

Clayton, C.R.I., Matthews, M.C., & Heymann, G. (2003). The chalk. In T. Tan, S. Phoon, D.W. Hight, & S. Leroueil (Eds.), *Proceedings of the International Workshop on Characterisation and Engineering Properties of Natural Soils* (pp. 983-1020), Singapore. CRC Press.

Cui, W., Potts, D.M., Pedro, A.M.G., & Zdravković, L. (2021). Numerical assessment of the effects of end-restraints and a pre-existing fissure on the interpretation of triaxial tests on stiff clays. *Géotechnique*, 71(9), 765-780. http://doi.org/10.1680/jgeot.19.P.318.

Davies, B.J., Roberts, D.H., Bridgland, D.R., Cofaigh, C.O., & Riding, J.B. (2011). Provenance and depositional environments of Quaternary sediments from the western North Sea Basin. *Journal of Quaternary Science*, 26(1), 59-75. http://doi.org/10.1002/jqs.1426.

Diambra, A., Ciavaglia, F., Harman, A., Dimelow, C., Carey, J., & Nash, D.F. (2014). Performance of cyclic cone penetration tests in chalk. *Géotechnique Letters*, 4(3), 230-237. http://doi.org/10.1680/geolett.14.00050.

Hight, D.W., & Jardine, R.J. (1993). Small strain stiffness and strength characteristics of hard London Tertiary clays. In A. Anagnostopoulos, F. Schlosser, N. Kalteziotis, & R. Frank (Eds.), *Geotechnical engineering of hard soils-soft rocks* (Vol. 1, pp. 533-552). Rotterdam: Balkema.

Jardine, R.J., Symes, M.J., & Burland, J.B. (1984). The measurement of soil stiffness in the triaxial apparatus. *Géotechnique*, 34(3), 323-340. http://doi.org/10.1680/geot.1984.34.3.323.

Jardine, R.J. (1985). *Investigations of pile-soil behaviour, with special reference to the foundations of offshore structures* [Doctoral thesis]. Imperial College, University of London, London, UK. Retrieved in August 23, 2023, from https://spiral.imperial.ac.uk/handle/10044/1/8519

Jardine, R.J. (1992). Some observations on the kinematic nature of soil stiffness. *Soil and Foundation*, 32(2), 111-124. http://doi.org/10.3208/sandf1972.32.2_111.

Jardine, R.J., Standing, J.R., & Kovacevic, N. (2005). Lessons learned from full scale observations and the practical application of advanced testing and modeling. In *Proceedings of the International Symposium on Deformation Characteristics of Geomaterials* (Vol. 2, pp. 201-245), Lyon. Lisse: Balkema. http://doi.org/10.1201/9780203970812.

Jardine, R.J., Standing, J.R., & Chow, F.C. (2006). Some observations of the effects of time on the capacity of piles driven in sand. *Géotechnique*, 56(4), 227-244. http://doi.org/10.1680/geot.2006.56.4.227.

Jardine, R.J., & Standing, J.R. (2012). Field axial cyclic loading experiments on piles driven in sand. *Soil and Foundation*, 52(4), 723-736. http://doi.org/10.1016/j.sandf.2012.07.012.

Jardine, R.J., Andersen, K., & Puech, A. (2012). Cyclic loading of offshore piles: potential effects and practical design. In *Proceedings of the 7th International Conference on Offshore Site Investigations and Geotechnics* (pp. 59-100). London: Society for Underwater Technology.

Jardine, R.J. (2014). Advanced laboratory testing in research and practice: the 2nd Bishop Lecture. *Geotechnical Research*, 1(1), 2-31. http://doi.org/10.1680/geores.14.00003.

Jardine, R.J. (2020). Geotechnics, energy and climate change: the 56th rankine lecture. *Géotechnique*, 70(1), 3-59. http://doi.org/10.1680/jgeot.18.RL.001.

Jardine, R.J. (2023a). Time-dependent vertical bearing behaviour of shallow foundations and driven piles: the 6th McClelland Lecture. In *Proceedings of the 9th International offshore Site Investigation and Geotechnics Conference*, London.

Jardine, R.J., Buckley, R.M., Liu, T., Byrne, B.W., Kontoe, S., McAdam, R.A., Schranz, F., & Vinck, K. (2023b). The ALPACA and ALPACA Plus Joint Industry studies of driven pile behaviour in low-to-medium density chalk. In *Proceedings of the 9th International offshore Site Investigation and Geotechnics Conference*, London.

Jardine, R.J., Buckley, R.M., Liu, T., Andolfsson, T., Byrne, B.W., Kontoe, S., McAdam, R.A., Schranz, F., & Vinck, K. (2023c). The axial behaviour of piles driven in chalk. *Géotechnique*, 1-17. In press. http://doi.org/10.1680/jgeot.22.00041.

Jefferies, M., & Been, K. (2015). *Soil liquefaction: a critical state approach*. Boca Raton: CRC Press. http://doi.org/10.1201/b19114.

Karlsrud, K., Jensen, T.G., Wensaas Lied, E.K., Nowacki, F., & Simonsen, A.S. (2014). Significant ageing effects for axially loaded piles in sand and clay verified by new field load tests. In *Proceedings of the Offshore Technology Conference* (Paper OTC-25197-MS), Houston, TX, USA. http://doi.org/10.4043/25197-MS.

Koseki, J. (2021). Several challenges in advanced laboratory testing of geomaterials with emphasis on unconventional types of liquefaction tests. *Geomechanics for Energy and the Environment*, 27, 100157. http://doi.org/10.1016/j.gete.2019.100157.

Kuwano, R. (1999). *The stiffness and yielding anisotropy of sand* [Doctoral thesis]. Imperial College London, London, UK. Retrieved in August 23, 2023, from https://spiral.imperial.ac.uk/handle/10044/1/8519

Kuwano, R., & Jardine, R.J. (2002). On the applicability of cross anisotropic elasticity to granular materials at very small strains. *Géotechnique*, 52(10), 727-749. http://doi.org/10.1680/geot.2002.52.10.727.

Lehane, B.M., Liu, Z., Bittar, E., Nadim, F., Lacasse, S., Jardine, R., Carotenuto, P., Rattley, M., & Gavin, K. (2020). A new 'unified' CPT-based axial pile capacity design method for driven piles in sand. In *Proceedings of the 4th International Symposium on Frontiers in Offshore Geotechnics* (pp. 462-477), Austin, TX, USA.

Lehane, B.M., Liu, Z., Bittar, E.J., Nadim, F., Lacasse, S., Bozorgzadeh, N., Jardine, R.J., Ballard, J.C., Carotenuto, P., Gavin, K., Gilbert, R.B., Bergan-Haavik, J., Jeanjean, P., & Morgan, N. (2022). CPT-based axial capacity design method for driven piles in clay. *Journal of Geotechnical and Geoenvironmental Engineering*, 148(9), 04022069. http://doi.org/10.1061/(ASCE)GT.1943-5606.0002847.

Liu, T. (2018). *Advanced laboratory testing for offshore pile foundations under monotonic and cyclic loading* [Doctoral thesis]. Imperial College London, London, UK. http://doi.org/10.25560/101146.

Liu, T., Chen, H., Buckley, R., Quinteros, S., & Jardine, R.J. (2019a). Characterisation of large-displacement interface shearing behaviour for application in design of steel piles driven in sands. In A. Tarantino, & E. Ibraim (Eds.), *Proceedings of the 7th International Symposium on Deformation Characteristics of Geomaterials*, Glasgow, UK. http://doi.org/10.1051/e3sconf/20199213001.

Liu, T., Quinteros, S., Jardine, R.J., Carraro, J.A.H., & Robinson, J. (2019b). A unified database of ring-shear interface tests on sandy-silty soils. In *Proceedings of the XVII European Conference on Soil Mechanics and Geotechnical Engineering (ECSMGE-2019)*, Reykjavik, Iceland. http://doi.org/10.32075/17ECSMGE-2019-0268.

Liu, T., Ushev, E.R., & Jardine, R.J. (2020). Anisotropic stiffness and shear strength characteristics of a stiff glacial till. *Journal of Geotechnical and Geoenvironmental Engineering*, 146(12), 04020137. http://doi.org/10.1061/(ASCE)GT.1943-5606.0002387.

Liu, T., Jardine, R.J., Vinck, K., & Ackerley, S.K. (2022a). Optimization of advanced laboratory monotonic and cyclic triaxial testing on fine sands. *Geotechnical Testing Journal*, 45(6), 1087. http://doi.org/10.1520/GTJ20210190.

Liu, T., Ahmadi-Naghadeh, R., Vinck, K., Jardine, R.J., Kontoe, S., Buckley, R.M., & Byrne, B.W. (2022b). An experimental investigation into the behaviour of de-structured chalk under cyclic loading. *Géotechnique*, 1-13. In press. http://doi.org/10.1680/jgeot.21.00199.

Liu, T., Ushev, E.R., & Jardine, R.J. (2023a). Anisotropy and cyclic loading characteristics of a stiff Bolders Bank glacial till at Cowden. In *Proceedings of the 8th International Symposium on Deformation Characteristics of Geomechanics (IS-Porto)*, Porto.

Liu, T., Ferreira, P.M.V., Vinck, K., Coop, M.R., Jardine, R.J., & Kontoe, S. (2023b). The behaviour of a low-to-medium density chalk under a wide range of pressure conditions. *Soil and Foundation*, 63(1), 101268. http://doi.org/10.1016/j.sandf.2022.101268.

Liu, T., Jardine, R.J., Vinck, K., Ahmadi-Naghadeh, R., Kontoe, S., Buckley, R.M., Byrne, B.W., & McAdam, R.A. (2023c). Cyclic characterisation of low-to-medium density chalk for offshore driven pile design. In *Proceedings of the 9th International offshore Site Investigation and Geotechnics Conference*, London.

Mao, X., & Fahey, M. (2003). Behaviour of calcareous soils in undrained cyclic simple shear. *Géotechnique*, 53(8), 715-727. http://doi.org/10.1680/geot.2003.53.8.715.

Muraro, S., & Jommi, C. (2019). Implication of end restraint in triaxial tests on the derivation of stress–dilatancy rule for soils having high compressibility. *Canadian Geotechnical Journal*, 56(6), 840-851. http://doi.org/10.1139/cgj-2018-0343.

Nishimura, S. (2014). Assessment of anisotropic elastic parameters of saturated clay measured in triaxial apparatus: appraisal of techniques and derivation procedures. *Soil and Foundation*, 54(3), 364-376. http://doi.org/10.1016/j.sandf.2014.04.006.

Ove Arup and Partners. (1988). *Research on the behaviour of piles as anchors for buoyant structures* (Offshore Technology Report, No. OTH 86 215). London: Department of Energy, 80 p.

Page, A.M., Klinkvort, R.T., Bayton, S., Zhang, Y., & Jostad, H.P. (2021). A procedure for predicting the permanent rotation of monopiles in sand supporting offshore wind turbines. *Marine Structures*, 75, 102813. http://doi.org/10.1016/j.marstruc.2020.102813.

Pedone, G., Kontoe, S., Zdravković, L., Jardine, R.J., Vinck, K., & Liu, T. (2023). Numerical modelling of laterally loaded piles driven in low-to-medium density fractured chalk. *Computers and Geotechnics*, 156, 105252. http://doi.org/10.1016/j.compgeo.2023.105252.

Powell, J.J.M., & Butcher, A.P. (2003). Characterisation of a glacial till at Cowden, Humberside. In T.S. Tan, K.K. Phoon, D.W. Hight, & S. Leroueil (Eds.), *Proceedings of the International Workshop on Characterisation and Engineering Properties of Natural Soils* (Vol. 2, pp. 983-1020), Singapore.

Rowe, P., & Barden, L. (1964). Importance of free ends in triaxial testing. *Journal of the Soil Mechanics and Foundations Division*, 90(1), 1-27. http://doi.org/10.1061/JSFEAQ.0000586.

Selby, M., Zhou, H., Liu, T., & Boylan, N. (2023). Back analysis of PISA pile tests at Dunkirk using a practical Nor-Sand model. In *Proceedings of the 9th International Conference on Offshore site Investigations and Geotechnics*. London: Society for Underwater Technology.

Taborda, D.M.G., Zdravkovic´, L., Kontoe, S., & Potts, D.M. (2014). Computational study on the modification of a bounding surface plasticity model for sands. *Computers* *and Geotechnics*, 59, 145-160. http://doi.org/10.1016/j.compgeo.2014.03.005.

Taborda, D.M.G., Zdravković, L., Potts, D.M., Burd, H.J., Byrne, B.W., Gavin, K.G., Houlsby, G.T., Jardine, R.J., Liu, T., Martin, C.M., & McAdam, R.A. (2020). Finite-element modelling of laterally loaded piles in a dense marine sand at Dunkirk. *Géotechnique*, 70(11), 1014-1029. http://doi.org/10.1680/jgeot.18.PISA.006.

Ushev, E.R. (2018). *Laboratory investigation of the mechanical properties of Cowden till under static and cyclic conditions* [Doctoral thesis]. Imperial College London, London, UK. http://doi.org/10.25560/78220.

Ushev, E.R., & Jardine, R.J. (2022a). The mechanical behaviour of Bolders Bank till. *Canadian Geotechnical Journal*, 59(12), 2163-2183. http://doi.org/10.1139/cgj-2021-0436.

Ushev, E.R., & Jardine, R.J. (2022b). The behaviour of Bolders Bank glacial till under undrained cyclic loading. *Géotechnique*, 72(1), 1-19. http://doi.org/10.1680/jgeot.18.P.236.

Vinck, K. (2016). *Laboratory testing of Dunkerque sand* [Master's dissertation]. Imperial College, London, UK..

Vinck, K., Liu, T., Ushev, E., & Jardine, R.J. (2019). An appraisal of end constraint effects on triaxial monotonic and cyclic tests on a range of geomaterials. In A. Tarantino, & E. Ibraim (Eds.), *Proceedings of the 7th International Symposium on Deformation Characteristics of Geomaterials*, Glasgow, UK. http://doi.org/10.1051/e3sconf/20199202007.

Vinck, K. (2021). *Advanced geotechnical characterisation to support driven pile design at chalk sites* [Doctoral thesis]. Imperial College, London, UK. Retrieved in August 23, 2023, from https://spiral.imperial.ac.uk/handle/10044/1/107416

Vinck, K., Liu, T., Jardine, R.J., Kontoe, S., Ahmadi-Naghadeh, R., Buckley, R.M., Byrne, B.W., Lawrence, J., Mcadam, R.A., & Schranz, F. (2022). Advanced in-situ and laboratory characterisation of the ALPACA chalk research site. *Géotechnique*, 1-15. In press. http://doi.org/10.1680/jgeot.21.00197.

Vinck, K., Liu, T., Mawet, J., Kontoe, S., & Jardine, R.J. (2023a). Field tests on large scale instrumented piles driven in chalk: results and interpretation. *Canadian Geotechnical Journal*, 60(10), 1475-1490. http://doi.org/10.1139/cgj-2022-0441.

Vinck, K., Liu, T., Jardine, R.J., Byrne, B.W., & Willow, A. (2023b). The effects of steel corrosion on the interface shearing behaviour of chalk. In *Proceedings of the 9th Int. Conf on Offshore site Investigations and Geotechnics.* London: Society for Underwater Technology.

Wen, K., Kontoe, S., Jardine, R.J., & Liu, T. (2023a). An axial load transfer model for piles driven in chalk. *Journal of Geotechnical and Geoenvironmental Engineering*, 149(11), 04023107. http://doi.org/10.1061/JGGEFK.GTENG-11368.

Wen, K., Kontoe, S., Jardine, R.J., Liu, T., & Pan, L. (2023b). Non-linear finite-element analysis of axially loaded piles driven in chalk. In L. Zdravković, S. Kontoe, D.M.G. Taborda, & A. Tsiampousi (Eds.), *Proceedings of the 10th European Conference on Numerical Methods in Geotechnical Engineering*, London. http://doi.org/10.53243/NUMGE2023-337.

Yang, Z.X., Guo, W.B., Jardine, R.J., & Chow, F. (2017). Design method reliability assessment from an extended database of axial load tests on piles driven in sand. *Canadian Geotechnical Journal*, 54(1), 59-74. http://doi.org/10.1139/cgj-2015-0518.

Zdravković, L., Jardine, R.J., Taborda, D.M.G., Abadias, D., Burd, H.J., Byrne, B.W., Gavin, K., Houlsby, G.T., Igoe, D., Liu, T., Martin, C.M., McAdam, R.A., Muir-Wood, A., Potts, D.M., Skov Gretlund, J., & Ushev, E. (2020a). Ground characterisation for PISA pile testing and analysis. *Géotechnique*, 70(11), 945-960. http://doi.org/10.1680/jgeot.18.PISA.001.

Zdravković, L., Taborda, D.M.G., Potts, D.M., Abadias, D., Burd, H.J., Byrne, B.W., Gavin, K., Houlsby, G.T., Jardine, R.J., Martin, C.M., McAdam, R.A., & Ushev, E. (2020b). Finite element modelling of laterally loaded piles in a stiff glacial clay till at Cowden. *Géotechnique*, 70(11), 999-1013. http://doi.org/10.1680/jgeot.18.PISA.005.

Zdravković, L., Potts, D.M., & Taborda, D.M.G. (2021). Integrating laboratory and field testing into advanced geotechnical design. *Geomechanics for Energy and the Environment*, 27, 100216. http://doi.org/10.1016/j.gete.2020.100216.